



Technische Universität München

Master Thesis

First Constraint on the Relic Neutrino Background with KATRIN Data

Author: Fabian Kellerer
Supervisor: Dr. Thierry Lasserre
Primary Reviewer: Prof. Dr. Susanne Mertens

*A thesis submitted in fulfillment of the requirements
for the degree of Master of Science*

in the

Professur für Dark Matter
Fakultät für Physik

November 3, 2021

Contents

Abstract	ix
1 Introduction and Theoretical Background	1
1.1 The Λ CDM Model	1
1.2 Theory of the Cosmic Neutrino Background	2
1.3 Observational Evidence for the Existence of Relic Neutrinos	5
1.4 Possible direct Detection Methods	6
1.4.1 High-Energy Scattering: Colliders and Cosmic Rays	6
1.4.2 Macroscopic Coherent Scattering	6
1.4.3 Capture on Radioactive Nuclei	7
1.5 Existing Experimental Limits on the Relic Neutrino Overdensity	7
2 Introduction to the KATRIN Experiment	9
2.1 Experimental Setup	10
2.1.1 Rear Section	10
2.1.2 WGTS	10
2.1.3 Transport Section	11
2.1.4 Pre- and Main Spectrometer	11
2.1.5 Focal Plane Detector (FPD)	12
2.2 First Measurement of the Neutrino Mass	12
3 Model of the Relic Neutrino Signal in KATRIN	15
3.1 Relic Neutrino Capture on Tritium Molecules	15
3.2 Modeling Assumptions	16
3.3 Position of the Relic Neutrino Signal in the Energy Spectrum	17
3.4 Differential Width of the Relic Neutrino Signal	19
3.5 Expected Rate of the Relic Neutrino Signal in KATRIN	19
3.5.1 Total Rate of Relic Neutrino Captures in the WGTS	20
3.5.2 FSD Losses	20
3.5.3 Zero Scattering Probability	21
3.5.4 Acceptance Angle of the Spectrometer	21
3.5.5 Detector Effects	21
3.5.6 Effective Tritium Mass and Expected Rate	21
3.6 Fit Model Including a Relic Neutrino Signal	22
4 Data Sets	25
4.1 KRN1 Measurement Campaign	25
4.1.1 KRN1 Configuration	25
4.1.2 KRN1 Expected Rate	25
4.2 KATRIN Design Monte Carlo Data Set	25

5	Analysis on Monte Carlo Simulations	29
5.1	KRN1 Monte Carlo Data Sets	29
5.1.1	Sensitivity Estimation of KRN1 Using Asimov Twins with Different True Neutrino Masses	29
5.1.2	Sensitivity Estimation of KRN1 with Fluctuated Twins	30
5.1.3	Systematics Breakdown Using KRN1 Twins	32
5.1.4	Prediction of the Exclusion Limit: Raster Scan Method	35
5.1.5	Prediction of the Exclusion Limit: 2D Scan	35
5.2	KATRIN Design Monte Carlo Data Set	36
5.2.1	Reevaluation of the KATRIN Final Sensitivity Limit	36
5.2.2	Systematics Breakdown Using KATRIN Design MC	36
5.3	Possible Optimizations	38
5.3.1	MTD	38
5.3.2	Atomic Tritium	38
5.3.3	Theoretical Limit of a KATRIN-Type Experiment	39
6	KRN1 Exclusion Limit of the Relic Neutrino Overdensity	41
6.1	Best Fit Values	41
6.2	Possible Dependencies of the Best Fit Values	42
6.3	Raster Scan	45
6.4	2D Scan	45
6.5	Systematics Breakdown	45
7	Conclusions and Outlook	49
	Acknowledgements	51
	Bibliography	53
A	Associated Code	57
B	Time-specific sub-samples of the KRN1 golden Run List	59
B.1	KNM1-FirstHalfTime (92 runs)	59
B.2	KNM1-MiddleHalfTime (91 runs)	59
B.3	KNM1-LastHalfTime (91 runs)	59

List of Figures

1.1	Predicted relic neutrino density in the Milky Way	4
2.1	Neutrino mass imprint in β decay electrons	9
2.2	Schematic view of the KATRIN beam line	10
2.3	Working principle of a MAC-E filter	13
3.1	FSD ground states	16
3.2	Relic neutrino signal over Background ratio vs. energy in KATRIN	17
3.3	Capture electron differential spectrum	18
3.4	Position of the relic neutrino peak relative to E_0	20
3.5	Impact of the fit parameters on the spectrum	24
4.1	MTDs of KATRIN nominal and KRN1	27
5.1	χ^2 profile example	30
5.2	η sensitivity of KRN1 twins	31
5.3	Example fit with random fluctuations	31
5.4	Distribution of the best fit values of η on fluctuated twins	32
5.5	Systematics breakdown of KRN1 Asimov twins	34
5.6	Raster scan of KRN1 Asimov twins	35
5.7	2D scan over m_ν^2 and η with KRN1 Asimov twins	36
5.8	η sensitivity of KATRIN design MC	37
5.9	Systematics breakdown of the KATRIN nominal MC	38
5.10	Proposed MTD optimization, compatible with neutrino mass measurements	39
5.11	η limit with atomic tritium	39
5.12	Optimized design MTD	40
6.1	Correlations of the fit parameters	42
6.2	KRN1 data best fit	43
6.3	p-value of the KRN1 data best fit	43
6.4	Spectrum and fit of PSR2 only	44
6.5	Raster scan over KRN1 data	45
6.6	2D scan over KRN1 data	46
6.7	η systematics breakdown on KRN1 data	47

List of Tables

3.1	Experimental yields for KATRIN nominal settings	22
4.1	Experimental yields in KATRIN for KRN1	26
4.2	Settings for KRN1 and KATRIN nominal simulations	26
5.1	Systematics budget for KRN1	33
5.2	Systematics for KRN1 Asimov twins	34
5.3	Systematics budget for the KATRIN nominal MC	37
5.4	Optimized KATRIN design η limits	40
6.1	Fit parameters on KRN1 data	42
6.2	Time dependent η fit values	42
6.3	η fit results, pseudo-ring wise	44

TECHNISCHE UNIVERSITÄT MÜNCHEN

*Abstract*Professur für Dark Matter
Fakultät für Physik

Master of Science

First Constraint on the Relic Neutrino Background with KATRIN Data

by Fabian Kellerer

The existence of a cosmic neutrino background (CνB, hereinafter also referred to as "relic neutrinos") produced around 1 s after the Big-Bang is a long standing prediction of the exceedingly successful Λ CDM model of cosmology. Although not designed for this task, the Karlsruhe TRITium Neutrino (KATRIN) experiment located in Karlsruhe, Germany is uniquely suited to set limits on the local density of relic neutrinos. Its intense tritium source allows interactions with the relic neutrino background via the reaction $\bar{\nu}_e + {}^3\text{H} \rightarrow {}^3\text{He}^+ + e^-$. This thesis aims to set a first upper limit on the dimensionless relic neutrino overdensity parameter η using KATRIN data. Additionally, an updated sensitivity limit of the KATRIN experiment is derived. A simplified model of the expected relic neutrino signal in KATRIN was developed and added to the tritium β decay model of the Samak analysis framework. The relic neutrino signal contains η as a free fit parameter. Using twin Monte Carlo data, the χ^2 profile of η is used to find the KATRIN sensitivity limit. The revised sensitivity limit of the KATRIN experiment is shown to be $\eta < 1 \times 10^{10}$, taking into account an updated background rate. Lastly, an upper limit on data using the first high-purity measurement campaign of KATRIN is derived, yielding $\eta < 7 \times 10^{11}$ at 99% confidence level.

Chapter 1

Introduction and Theoretical Background

1.1 The Λ CDM Model

The Λ CDM model is the most widely recognized model for explaining the evolution and the large-scale structure of the universe. The discussion here excludes the inflationary period, up to 1×10^{-30} s after the Big-Bang, which is not relevant to this work. Within those bounds, the Λ CDM model describes a universe consisting of vacuum energy, matter (cold dark matter and ordinary matter) and radiation. Each constituent has an associated dimensionless density parameter, Ω_Λ , Ω_m and Ω_{rad} . All three are assumed to be perfect fluids with an equation of state $p = w\rho$, where matter has $w = 1/3$, radiation $w = 1/3$ and the vacuum energy $w = -1$. The metric of the universe is of the Friedmann-Robertson-Walker (FRW) form:

$$ds^2 = dt^2 - R_0^2 \cdot a(t)^2 \cdot \left[\frac{dr^2}{1 - kr^2} + r^2 (d\theta^2 + \sin^2\theta d\phi^2) \right] \quad (1.1)$$

Here, a is the time-dependent scale factor of the universe, R_0 the scale of the universe today, and r, θ, ϕ the so-called comoving coordinates. The curvature parameter k is assumed to be zero in the Λ CDM model (measurements have put an upper bound of 10^{-3} on this parameter [30]). From this and the Einstein field equations, the Friedmann equations can be derived, which are the basic equations that describe the evolution of the universe given the initial density parameters in the Λ CDM model:

$$H(t) = \frac{\dot{a}}{a} = \sqrt{\frac{8\pi G}{3} \cdot (\rho_{\text{rad}} + \rho_{\text{matter}}) + \frac{\Lambda}{3}} = H_0 \sqrt{\Omega_m a^{-3} + \Omega_{\text{rad}} a^{-4} + \Omega_\Lambda} \quad (1.2)$$

For a universe with $k=0$, there are only solutions that expand forever, no matter the composition of the universe. For radiation and matter dominated universes, the expansion approaches zero for $t \rightarrow \infty$, whereas for a universe where vacuum energy is dominant, the expansion speeds up. Additionally, the radiation and matter densities are inversely proportional to a^4 and a^3 respectively, whereas Ω_Λ stays constant with respect to a . In the Λ CDM model, our universe went through three phases with different dominant species: The radiation density has the strongest dependence on a , so the first phase after the Big-Bang was radiation dominated. After that, matter took over as the dominant force, but its influence diminishes as well like a^{-3} , so eventually the vacuum energy became the dominant factor, speeding up the expansion of the universe even more. Today it is estimated that

$\Omega_\Lambda \approx 0.7$, $\Omega_m \approx 0.3$ and Ω_{rad} is negligible.

1.2 Theory of the Cosmic Neutrino Background

At less than 1 s after the Big-Bang, neutrinos were in equilibrium with the plasma via weak interactions:

$$\begin{aligned} \nu_l \bar{\nu}_l &\leftrightarrow l^+ l^- \\ \nu_e &\leftrightarrow e^- \end{aligned}$$

Neutrinos are fermions, and therefore follow a Fermi-Dirac distribution:

$$f_\nu(\vec{p}, t) = \frac{g_\nu}{e^{\frac{E_\nu(\vec{p}) - \mu_\nu(t)}{k_B T(t)} + 1}} \quad (1.3)$$

Here, g_ν is the number of degrees of freedom, E_ν the neutrino energy and μ_ν the chemical potential, which is zero in the early universe if the Lepton number is a lot smaller than the number of photons (since $\mu_{\text{particle}} = -\mu_{\text{antiparticle}}$ in equilibrium with photons). Since relic neutrinos have not been directly measured yet, this has to be assumed. The neutrino number density follows from integrating Eq. 1.3 over the energy, yielding

$$n_\nu \propto T^3 \quad (1.4)$$

and

$$\frac{n_{\text{Fermion}}}{n_{\text{Boson}}} = 3/4 \quad (1.5)$$

in the relativistic limit. This means that the neutrino reaction rate Γ decreases with the temperature like T^5 [9]:

$$\Gamma = n_\nu \langle \sigma v \rangle \approx T^3 G_F T^2 = G_F T^5 \quad (1.6)$$

As the universe expanded, it cooled down, eventually leading to a decoupling of the neutrinos from the plasma. The neutrino number density and energy distribution were subsequently frozen and only influenced by the expansion of the universe. This decoupling happened roughly around the time when the Hubble parameter grew larger than the neutrino reaction rate, at a time when the universe was still radiation dominated [9]. Therefore, Eq. 1.2 in the radiation-dominated limit and the Stefan-Boltzmann law ($\rho_{\text{rad}} \propto T^4$) can be used to deduce the temperature dependence of the Hubble parameter:

$$H \propto \sqrt{\rho_{\text{rad}}} \propto T^2 \quad (1.7)$$

Using this and Eq. 1.6, the temperature of neutrino decoupling is around 1 MeV [9]. From Eq. 1.2 and 1.7, the relation between T and t and subsequently the time of neutrino decoupling can be derived:

$$H = \frac{\dot{a}}{a} = H_0 \sqrt{\Omega_{\text{rad}} a^{-4}} \propto \frac{1}{a^2} \Rightarrow H \propto 1/t \quad (1.8)$$

$$\Rightarrow T \propto \frac{1}{t^{1/2}} \propto \frac{1}{a} \quad (1.9)$$

An exact derivation gives a decoupling time of around 1 s after the Big-Bang [9].

To get the neutrino temperature and number density today, they can be expressed in terms of the temperature and number density of the CMB, which have been measured to great precision: the relation $T \propto 1/a$ from Eq. 1.9 is applicable as long as the number of relativistic degrees of freedom $g_*(T)$ in the plasma does not change. Generally, for a plasma consisting of Bosons and Fermions, g_* takes the form:

$$g_*(T) = \sum_{\text{Bosons}} g_{\text{Boson}} + \frac{7}{8} \sum_{\text{Fermions}} g_{\text{Fermion}} \quad (1.10)$$

The neutrino decoupling happens shortly before the electron-positron annihilation $e^+e^- \rightarrow \gamma\gamma$ (when the mean photon energy drops below $2m_e \approx 1$ MeV), which does change g_* . Consequently, the neutrino and photon temperatures differ by a factor of $\left(\frac{g_{*,2}}{g_{*,1}}\right)^3$, with $g_{*,1}$ and $g_{*,2}$ being the number of degrees of freedom before and after electron-positron annihilation. After electron-positron annihilation, $g_{*,2} = 2$, while before, $g_{*,1} = 2 + 7/8 \cdot (2 + 2) = 11/2$, from electrons, positrons and photons. It follows that

$$T_\nu = \left(\frac{4}{11}\right)^3 \cdot T_\gamma = 1.95 \text{ K} \quad (1.11)$$

It has to be noted that this is only valid if the neutrinos stay relativistic until today. This is the case for $m_\nu < k_B T_\nu = 1.7 \times 10^{-4}$ eV. However, neutrino oscillations of atmospheric and solar neutrinos imply that at least two mass eigenstates are non-relativistic today [11]

Finally, the total number of relic neutrinos stayed constant after neutrino decoupling, and the amount of photons stayed constant after electron-positron annihilation ($e^- + p \rightarrow H + \gamma$ negligible). Using this, as well as Eq. 1.4 and 1.5, the relic neutrino number density for one neutrino (or antineutrino) species today is

$$\bar{n}_\nu = \frac{1}{2} \cdot \frac{3}{4} \cdot \left(\frac{T_\nu}{T_\gamma}\right)^3 \cdot n_\gamma = 56 \frac{1}{\text{cm}^3} \quad (1.12)$$

This is an average across the entire universe, however if the neutrinos are non-relativistic today, they are most likely unevenly distributed, i.e. they would cluster around large masses such as galaxies. To describe this, a new parameter is introduced, the dimensionless local relic neutrino overdensity η :

$$\eta = \frac{n_\nu}{\bar{n}_\nu} = \frac{n_\nu}{56} \text{ cm}^3 \quad (1.13)$$

There are several theoretical predictions on this clustering in the literature: A very comprehensive study has been conducted by Ringwald and Wong [25], who model the relic neutrinos as a collisionless, weakly interacting gas whose phase space distributions $f_i(\vec{x}, \vec{p}, \tau)$ follow the Vlasov equation [25]:

$$\frac{Df_i}{D\tau} = \frac{\partial f_i}{\partial \tau} + \dot{\vec{x}} \cdot \frac{\partial f_i}{\partial \vec{x}} + \dot{\vec{p}} \cdot \frac{\partial f_i}{\partial \vec{p}} = 0 \quad (1.14)$$

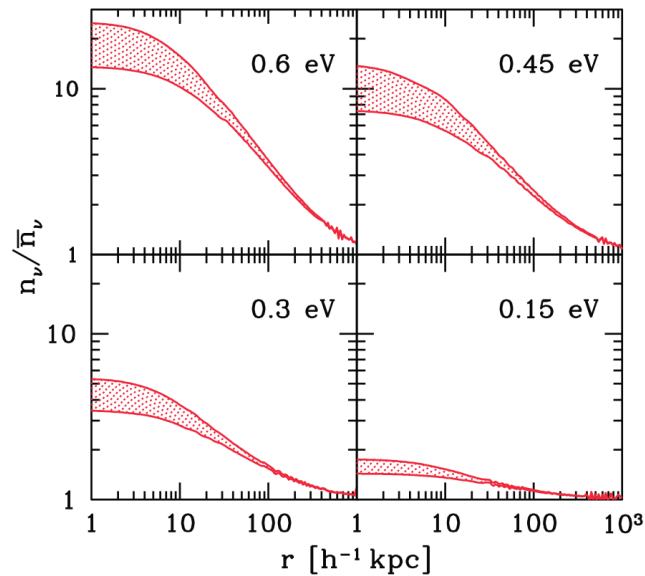


Figure 1.1: Relic neutrino overdensity n_ν/\bar{n}_ν , vs. distance from the galactic center in $h^{-1}\text{kpc}$ (h dimensionless and of order 1) for different neutrino masses. The curves are normalized to $\bar{n}_\nu = 56 \frac{1}{\text{cm}^3}$. The earth is located at $r \approx 10 h^{-1}\text{kpc}$. The top curve in each plot represents the simulation using the present day density profile of the Milky Way. Notably, the top left neutrino mass is within reach of the KATRIN experiment. Figure taken from [25]

The neutrinos gravitate around a mass distribution modeled after the Milky Way, for which they consider two density profiles: A universal parametrization of dark matter halos introduced by Navarro, Frenk and White called NFW profile [22], which can be used to describe young galaxies, and the current density profile of the Milky Way [25]. In reality, the density profile of the Milky Way transitioned smoothly from the NFW case to the present day density profile, however Ringwald and Wong performed two separate simulations for both cases to obtain upper and lower bounds on η [25]. The simulation was performed only for redshifts $z \leq 3$, because the relic neutrino velocity dispersion needs to drop below those of galaxies in order to cluster around them, which would be the case for $z \leq 2$ in the considered neutrino mass range [25]. For neutrino masses below 0.6 eV, they arrived at $\eta \leq 20$ [25]. Their results for the Milky Way are shown in Fig. 1.1. Other analyses include e.g. [20] by Lazauskas et al., where the authors assumed a constant ratio of baryon to neutrino density across the universe, leading to larger overdensities in the range of $10^3 - 10^4$. Even larger overdensities are considered by Stephenson et al. in [29], where the authors propose a light scalar boson that can interact with neutrinos, allowing in principle arbitrarily large overdensities if this new interaction is strong enough. It has to be mentioned, though, that very large overdensities can quickly come into conflict with other limiting factors such as the local dark matter density or the Pauli exclusion principle. The local dark matter density is generally estimated to be at least $0.2 \text{ GeV}/\text{cm}^3$ [23], which translates to a maximally allowed neutrino overdensity of $\eta \approx 6 \times 10^5$ for a neutrino mass

of 1 eV. The Pauli exclusion principle proves to be similarly restrictive: under the assumption that the relic neutrinos behave like an ideal Fermi gas, the densest possible clustering depends on the Fermi energy E_F according to Eq. 1.15.

$$n_\nu^{\max} = \frac{1}{3\pi^2} \cdot \left(\frac{2m_\nu E_F}{\hbar^2} \right)^{3/2} \quad (1.15)$$

There are several ways to assume a Fermi energy for the relic neutrinos. Here, the Milky Way escape energy and the mean kinetic energy of relic neutrinos today are investigated. The densest clustering around the Milky Way due to gravitational forces is naturally limited by the escape velocity of our galaxy, around 500 km/s. For neutrinos with a mass of 1 eV, this is equivalent to a Fermi energy of $1.4 \mu\text{eV}$. Applying Eq. 1.15 and dividing the result by the mean neutrino density per species, 56 cm^{-3} , gives an allowed overdensity of less than 400. However, this Fermi energy is significantly smaller than the assumed mean kinetic energy of the relic neutrinos today (0.2 meV). For the densest possible clustering, the momentum distribution approaches a step function that is zero for all momenta above the Fermi momentum. Since the mean of a step function is just the step position divided by two, the Fermi energy can be approximated as twice the mean, or 0.4 meV. This would allow overdensities of up to 5×10^6 . In any case, these astrophysical constraints are way more stringent the limits set by any experiment conducted so far (cf. Sec. 1.5).

1.3 Observational Evidence for the Existence of Relic Neutrinos

Apart from being a firm prediction of the most successful cosmological model to date, there are also empirical hints towards the existence of relic neutrinos. Firstly, there is the abundance of Helium in the universe, which is dependent on the number ratio of neutrons to protons, n_n/n_p during the Big-Bang nucleosynthesis (BBN). This ratio is fixed after the freeze-out of the weak interactions $n + e^+ \leftrightarrow p$ and $p + e^- \leftrightarrow n$ that keep protons and neutrons in equilibrium [12]. The freeze-out temperature T_{freeze} is determined by g_* , which is altered by the presence of neutrinos and can be used to set a limit on the number of relic neutrino species. Existing limits based on this method are generally not consistent with zero, but are quite dependent on model assumptions [12]. Data on the large-scale structure of the universe can also be used to probe the neutrino mass from relic neutrinos, however this again depends on a good understanding of the process of structure formation [12]. Lastly, the power spectrum of anisotropies in the CMB can provide evidence for the existence of relic neutrinos as well [25] [12]. While this provides solid evidence for the existence of the CνB, it does so exclusively at early stages of the evolution of the universe, and also only indirectly.

1.4 Possible direct Detection Methods

A direct detection of the elusive relic neutrinos is one of the most challenging undertakings of modern experimental physics, due to their very low kinetic energy and the feeble strength of the weak interaction. Nevertheless, there are several proposed methods that could be attempted to set boundaries on the local neutrino overdensity, and also some existing limits from earlier experiments.

1.4.1 High-Energy Scattering: Colliders and Cosmic Rays

This is what could be called the "brute force" method: In order to get around the exceedingly low kinetic energy of the relic neutrinos, they would be bombarded with highly energetic particles to provide the necessary threshold energy for reactions. The weak interaction cross section is growing with the center-of-mass energy below the W and Z resonances [24]. So, higher energies provide more favorable conditions for detection. The optimal beam particle to use would be heavy ions due to their inverse beta decay interaction channel that increases the overall reaction rate with relic neutrinos. Additionally, the inverse beta decay changes the charge of the daughter nucleus, leading to a change of trajectory in the accelerator, which would make the daughter nuclei detectable [24]. This would also allow an unambiguous proof that a neutrino was involved in the reaction. Still, the reaction rate in the LHC, the most powerful existing particle accelerator, is only of the order of $1 \times 10^{-5} \text{ yr}^{-1} \cdot \eta$, and even a theoretical accelerator around the entire earth would only deliver 10 reactions per year times η at energies of $1 \times 10^7 \text{ TeV}$ [24]. However, high-energy cosmic rays provide a very promising alternative. Resonant annihilation of high-energy neutrinos with relic antineutrinos into a Z -Boson provides two possible detection methods [24]: one can search for absorption dips at the resonant energies in the spectrum of high-energy neutrinos with experiments such as IceCube [15] or the upcoming KM3Net [19], or for Z -bursts caused by the decaying Z -Boson producing protons and photons above the predicted Greisen-Zatsepin-Kuzmin cutoff. The required neutrino energies would be [24]

$$E_{\nu_i}^{\text{res}} = \frac{m_Z^2}{2m_{\nu_i}} \approx 4 \cdot 10^{21} \left(\frac{\text{eV}}{m_{\nu_i}} \right) \text{eV} \quad (1.16)$$

Current experiments are sensitive in this energy range, and in the most optimistic case, the upcoming JEM-EUSO experiment [16] could already find evidence of absorption dips and Z -bursts. At the moment, this is the most promising prospect of finding direct evidence of relic neutrinos in the not too distant future [24].

1.4.2 Macroscopic Coherent Scattering

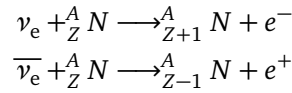
The exceedingly low momentum of present-day relic neutrinos leads to a de-Broglie wavelength of macroscopic scale [24]:

$$\lambda = 1/\langle p \rangle = 0.12 \text{ cm}/\langle p/T_{\nu,0} \rangle \quad (1.17)$$

This means that relic neutrinos could scatter coherently with a large number of target atoms, leading to a huge increase in the elastic scattering cross section [24]. The earth is moving with respect to the relic neutrino background (which should be at rest with respect to the Milky Way), so objects on Earth are expected to experience an acceleration due to the relic neutrino wind. For an optimally designed target and Dirac neutrinos, accelerations of up to $1 \times 10^{-28} \text{ cm/s}^2 \cdot \eta$ can be reached [24]. There are proposed experiments capable of measuring accelerations as small as $1 \times 10^{-23} \text{ cm/s}^2$, which is still considerably off from the prediction [24]. However, future developments might improve this.

1.4.3 Capture on Radioactive Nuclei

Lastly, relic neutrinos can still interact with regular matter provided the threshold energy for the reaction is close to zero. Neutrino capture on β -decaying nuclei fulfills this requirement:



A prior study by Hódak et al. [13] focused on two nuclei in particular, as they were a part of major upcoming experiments at the time: tritium in case of the KATRIN experiment and rhenium for MARE [28]. They found reaction rates per nucleon of $4.2 \times 10^{-25} \text{ yr}^{-1} \cdot \eta \cdot \epsilon$ for tritium and $2.75 \times 10^{-32} \text{ yr}^{-1} \cdot \eta \cdot \epsilon$ for rhenium ($\epsilon = 1$ for Majorana, $\epsilon = 1/2$ for Dirac neutrinos) [13]. Scaled up to the expected amounts of tritium and rhenium in the two experiments, the expected capture rates would be only $2.2 \times 10^{-5} \text{ yr}^{-1} \cdot \eta$ in KATRIN [7], and $6.7 \times 10^{-8} \text{ yr}^{-1} \cdot \eta$ in MARE [13]. This is before losses in the experiment are taken into account. While rhenium seems to be the less favorable option at first glance, Hódak et al. argue that such an experiment could be scaled up way more easily than a tritium source like KATRIN. A detection using a radioactive target also has the drawback of having a large background of β electrons that would have to be distinguished from the signal. In theory, the relic neutrino signal should be separated by the β endpoint by $2m_\nu$, however an experiment would need extraordinarily good energy resolution to resolve this difference [13]. While a detection using this method is therefore not expected, it has the advantage of having running experiments and data ready to go that can be used to set limits on η .

1.5 Existing Experimental Limits on the Relic Neutrino Overdensity

There are very few existing limits on η . Three will be presented here. Predecessor experiments of KATRIN have tried to explain anomalies in their measured tritium spectrum with relic neutrino capture, namely the Los Alamos [26] and Troitsk ν mass [21] experiments, which both found significantly negative best fit values of m_ν^2 . The Los Alamos analysis concluded that a relic neutrino overdensity of $\eta \geq 2 \cdot 10^{14}$ could explain their results, but acknowledged that this is way above any predicted value [26]. The

Troitsk experiment found a sinusoidal time dependence of their neutrino mass fit with a six month period, leading to a limit of $\eta \geq 1 \times 10^{13}$, as well as possible conclusions about the shape of the dense neutrino cloud. In this scenario, the earth would pass through a flattened, disc-shaped neutrino cloud, which is inclined relative to the ecliptic plane, twice a year [21]. Such large density fluctuations over small distances compared to the galactic scale are not expected in most models [25], and Lobashev et al. explain that this is a highly speculative scenario, which would need extensive experimental evidence and theoretical backing [21]. Further measurements at a similar experiment in Mainz indicate that the Troitsk anomaly is most likely an experimental artifact [7]. Finally, Hwang et al. [14] present an upper limit derived from cosmic rays: analogous to the GZK cutoff in the cosmic ray energy spectrum, there should be another cutoff due to the reaction $p + \nu_e \rightarrow n + e^+$. They cite a value of $\eta \geq 1 \times 10^{13}$ which should have a measurable impact on the spectrum [14]. The aforementioned Z-bursts are also considered as an explanation for flux above the GZK cutoff, giving limits in the range of $\eta \geq 1 \times 10^{14}$ [14].

Chapter 2

Introduction to the KATRIN Experiment

The KARlsruhe TRItium Neutrino Experiment (KATRIN) in Karlsruhe, Germany is an experiment designed for the direct measurement of the electron anti neutrino mass. It uses the kinematics of tritium beta decay, much like predecessor experiments in Los Alamos [26], Mainz [31] and Troitsk [21]:



Rather than searching for the weakly interacting neutrino itself, KATRIN measures the energy of the electrons from the decay. The non-zero neutrino mass leads to a kink-like distortion in the electron energy spectrum near its endpoint, as shown in Fig. 2.1. Because the neutrino mass and flavor eigenstates are not equal, experiments of this type are sensitive to a superposition of mass eigenstates:

$$m^2(\nu_e) = \sum_{i=1}^3 |U_{ei}|^2 \cdot m_i^2 \quad (2.2)$$

KATRIN aims to improve the neutrino mass limit from direct measurements by an order of magnitude, from 2 eV down to 0.2 eV [7]. Its first neutrino mass result in 2019 almost halved the previous limit down to 1.1 eV [3], and the second measurement campaign was able to set the first sub-eV limit for direct neutrino mass measurements [2].

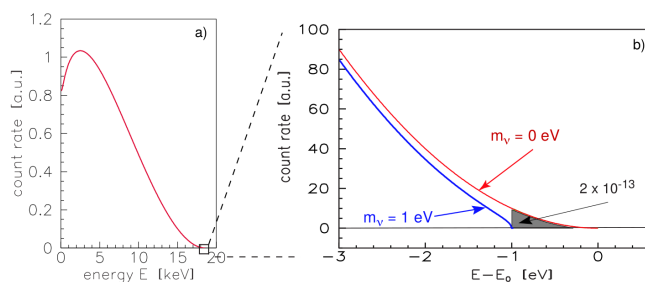


Figure 2.1: Electron energy spectrum of tritium β decay, for neutrino masses of 0 and 1 eV. The effect only becomes visible near the endpoint. Figure taken from [7]

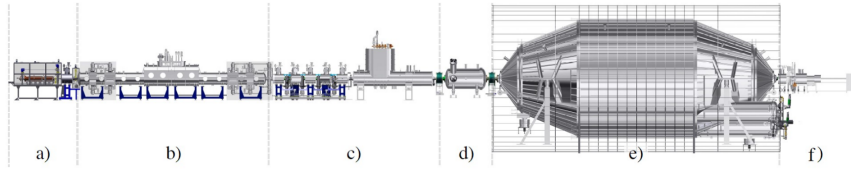


Figure 2.2: Schematic view of the KATRIN beam line. The major components are: a) the rear section, b) the windowless gaseous tritium source (WGTS), c) the transport section for tritium removal, d) and e) the pre- and main spectrometer and f) the detector. Figure adapted from [3]

2.1 Experimental Setup

KATRIN consists of different parts, assembled along a 70 m long axis, which are depicted in Fig. 2.2. From the most upstream towards the most downstream component along the beam line, they are: the rear section, which performs essential diagnostics tasks to keep the source stable (Sec. 2.1.1), the tritium source WGTS (Sec. 2.1.2), the transport section (Sec. 2.1.3), the two spectrometers (Sec. 2.1.4) and the detector (Sec. 2.1.5).

2.1.1 Rear Section

The rear section, located upstream of the WGTS, houses vital diagnostics and calibration devices. A rear detector is installed to monitor the source activity, as well as an electron gun that can be used not only for studying systematic effects, but is indispensable for accurately determining the KATRIN response function. Additionally, the rear wall of the WGTS can be set to non-zero potentials to control plasma effects in the WGTS [7].

2.1.2 WGTS

The windowless gaseous tritium source (WGTS), stretching over a length of 10 m, provides molecular tritium that emits the β decay electrons for the neutrino mass measurements in KATRIN. It contains cryogenic tritium gas cooled to 27 K, at a nominal column density of up to 5×10^{17} mol/cm² and a purity of more than 95% [7]. The impurities are mainly deuterium and hydrogen. In the KATRIN source, tritium is present in molecular form, bound either to another tritium (TT), a deuterium (DT) or a hydrogen atom (HT). The tritium is injected in the middle and diffuses to both ends of the WGTS, where it is pumped out again. This way, tritium is continuously cycled through the beam tube, with each molecule only traveling for about 1 s through the WGTS [7]. With a source diameter of 90 mm, the total activity of the WGTS at full column density is almost 1×10^{11} Bq [7].

The decay electrons are guided adiabatically to both ends of the source by a strong magnetic field with a nominal strength of 3.6 T. The column density and hence the gas inlet pressure has to be known to a precision of 0.1%, and the source temperature is required to be constant to 30 mK.

2.1.3 Transport Section

Since the WGTS is a windowless source, the tritium flow at the outlet pointing towards the spectrometers would cause significant background from β decays inside the spectrometers. To remedy this, the tritium flow at the end of the WGTS has to be suppressed by a factor of 10^{11} , leading to a background from β decays beyond the source of less than 1×10^{-3} cps [7]. This is done in the transport section, which consists of a differential (DPS) and cryogenic (CPS) pumping section. The DPS operates using turbomolecular pumps, while the CPS uses an extremely cold argon frost layer, cooled by liquid helium to 4.5 K, so that the tritium molecules are passively adsorbed onto the walls [7]. This is encouraged by kinks in the beam tube, through which the electrons can be guided by magnetic fields, while the neutral tritium molecules or ions follow different trajectories and hit the walls.

2.1.4 Pre- and Main Spectrometer

There are two spectrometers in the KATRIN experiment, which are of the MAC-E (Magnetic Adiabatic Collimation with Electrostatic filter) type [7]. They use an electric field along the beam axis as a high-pass filter to analyze the kinetic energy of the electrons. This is shown in green in Fig. 2.3. Such a field is only sensitive to the electron energy component parallel to the magnetic field lines, E_{\parallel} . However, incoming electrons have randomly distributed momenta, performing cyclotron motion around the guiding magnetic field, which is shown in blue in Fig. 2.3. It is therefore necessary to collimate the electron momenta along the magnetic field. In the KATRIN main spectrometer, this is done by reducing the guiding magnetic field by four orders of magnitude over a long distance, such that the magnetic field gradient across a single cyclotron orbit is negligible. This allows the electrons to move adiabatically and the magnetic moment μ is conserved [7]:

$$\mu \approx \frac{E_{\perp}}{|\vec{B}|} \approx \text{const.} \quad (2.3)$$

It follows from Eq. 2.3 that a reduction of $|\vec{B}|$ leads to a proportional reduction of the transversal energy component E_{\perp} . Since this happens adiabatically, the transversal energy is transformed into longitudinal energy that is sensitive to the electrostatic filter potential, as shown at the bottom of Fig. 2.3. The minimum of the magnetic field strength coincides with the maximum of the electric potential at the so-called analyzing plane, where E_{\perp} is minimal. The energy resolution of a MAC-E filter is limited by its capacity to minimize the transversal electron motion at the analyzing plane [7]:

$$\frac{\Delta E}{E} = \frac{B_{\text{ana}}}{B_{\text{max}}} \quad (2.4)$$

A better energy resolution requires a larger magnetic field gradient between the analyzing plane field B_{ana} and the inlet (pinch field, B_{max}). The pinch magnetic field B_{max} has a nominal value of 6 T, and the analyzing plane fields for pre- and main spectrometer are $B_{\text{ana}}^{\text{pre}} = 2 \times 10^{-2}$ T and $B_{\text{ana}}^{\text{main}} = 3 \times 10^{-4}$ T [7]. Consequently, the main spectrometer has an energy resolution of 0.93 eV around the endpoint energy of 18.5 keV. Downstream from

the analyzing plane, the electrons are re-accelerated towards the detector, and the magnetic field is increased again. To ensure adiabaticity along both magnetic field gradients, the main spectrometer has a length of 23 m. Since the magnetic flux along the beam line is constant, a lower field strength leads to an expansion of the electron beam, requiring especially the main spectrometer to be significantly bigger than the source and transport section beam tubes.

The largest part of the decay electrons are uninteresting for the neutrino mass analysis, as the impact of a non-zero neutrino mass is only visible at high electron energies very close to the endpoint. Therefore, the small pre-spectrometer is installed in front of the main spectrometer to veto electrons with energies below 18.3 keV. This reduces the flow rate by 10^{-6} and helps to prevent ionization of residual gas in the main spectrometer, which can contribute to the background [7]. Another electron veto is used to reject electrons with very large emission angles relative to the beam line. Such electrons have spent more time inside the source, which increases the likelihood of scattering. The maximally allowed angle of acceptance θ_{\max} can be tuned by setting the source magnetic field B_S to a lower value than B_{\max} [7]:

$$\theta_{\max} = \arcsin \sqrt{\frac{B_S}{B_{\max}}} \quad (2.5)$$

Electrons with larger emission angles are reflected back to the source due to the magnetic mirror effect.

The retarding potential of the main spectrometer is varied over time according to the measurement time distribution (MTD) of the specific run. The MTD contains a set of retarding potentials (also called HV set points), as well as a measurement time allocated to each HV set point (shown e.g. in Fig. 4.1). This time is highest near the endpoint where the neutrino mass signal is the strongest. The retarding potential steps through the MTD in alternating direction, allowing for an integral measurement of the electron count rate vs. electron energy. A full scan over the measurement time distribution is called a 'run' and is assigned a unique run number.

2.1.5 Focal Plane Detector (FPD)

The electron detector does not measure the energy of the impinging electrons, but their count rate. It is a silicon semiconductor detector consisting of 148 pixels arranged in 14 rings around the center. The segmentation allows to correct for inhomogeneities in the source or the magnetic and electric fields. After they have passed the main spectrometer, the electrons are post accelerated by several keV towards the detector to improve detection efficiency. With this, a detection efficiency of 95 % can be reached.

2.2 First Measurement of the Neutrino Mass

The first measurement campaign of KATRIN for which a neutrino mass analysis was finalized and published took place from April 10 to May 13, 2019 (cf. [3]). Due to radiochemical reactions of tritium with the previously unexposed injection capillary, the column density was kept at 1/5 of the nominal value [3].

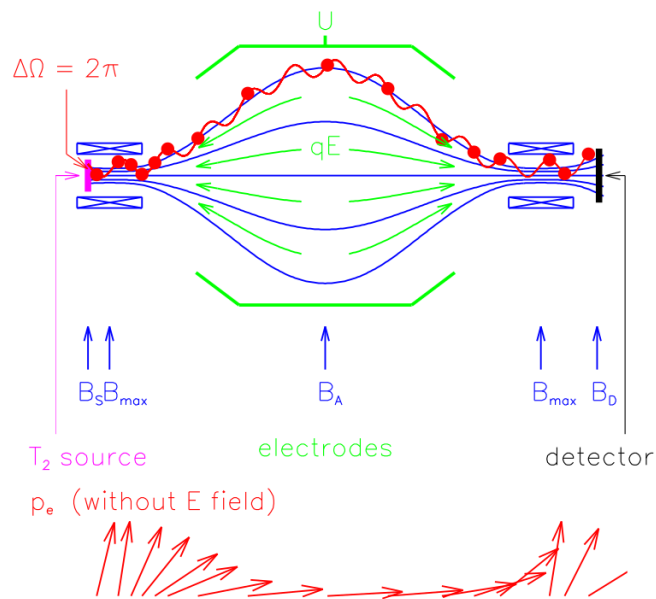


Figure 2.3: Working principle of a MAC-E filter: electric field lines in green, magnetic field lines in blue, electron path in red. At the bottom, the momentum transformation of an electron is visualized (without the electric field). Figure adapted from [7]

The neutrino mass analysis (KATRIN Neutrino Mass 1, 'KNM1') gives a best fit neutrino mass of $(-1_{-1.1}^{+0.9}) \text{ eV}^2$, from which an upper limit of $m_\nu \leq 1.1 \text{ eV}$ at 90% C.L. can be derived [3]. At the time, this represented a new record for direct kinematic measurements of the neutrino mass [3].

Chapter 3

Model of the Relic Neutrino Signal in KATRIN

3.1 Relic Neutrino Capture on Tritium Molecules

The relic electron anti neutrinos are able to interact weakly with radioactive tritium nuclei in the KATRIN source, triggering a neutrino-capture reaction:



This is possible since tritium can decay spontaneously, so this reaction has no threshold energy and can be triggered even by the very low-energy relic neutrinos. This reaction has a two-body final state, so the electron differential energy spectrum is just a singular peak at $2m_\nu$, above the endpoint of the β decay spectrum. Unless stated otherwise, all numbers and results in this work are given for Majorana neutrinos. As mentioned above, Dirac neutrinos interact at half the rate that Majorana neutrinos do. The cross section for this reaction is $\sigma_\nu = 7.84 \times 10^{-45} \text{ cm}^2$ [6] and the capture rate on a single tritium atom can be calculated with Eq. 3.2.

$$R_\nu = n_\nu \frac{N_A M_T}{3} \cdot \int \sigma_\nu v_\nu f(p_\nu) \frac{d^3 p_\nu}{2\pi^3} \quad (3.2)$$

Here, n_ν is the relic neutrino number density, N_A is the Avogadro constant, M_T is the mass of a tritium atom, v_ν and p_ν are the velocity and momentum of the relic neutrinos and $f(p_\nu)$ the momentum distribution [17].

Assuming a Fermi-Dirac distribution for $f(p_\nu)$, one arrives at a capture rate on a single tritium nucleus of $R_\nu = 4.2 \times 10^{-25} \text{ yr}^{-1}$ (without taking into account any experimental losses, cf. Tab. 3.1).

The differential energy spectrum of the electrons emitted after a relic neutrino capture reaction ("capture electrons") is further complicated for molecular tritium, because some of the energy released in the decay is lost to excitations of the molecular bond. In fact, β decay electrons face the same problem. So for the neutrino mass analysis, a molecular final state distribution (FSD) of the form $P_f(E_f)$ is used, giving an excitation probability P_f dependent on the excitation energy E_f , with E_f given relative to the recoil energy of a ${}^3\text{HeT}^+$ molecule [18]. Applying the same treatment to the capture electrons, their differential spectrum is the convolution of the intrinsic singular peak with an FSD $P_{f,\text{capture}}(-E_{f,\text{capture}})$.

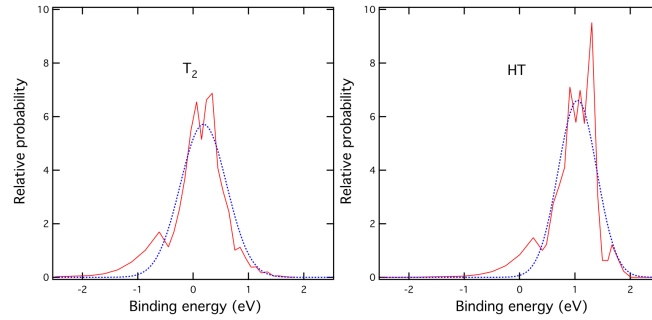


Figure 3.1: FSD ground states calculated from zero point motion in the parent molecule (blue dotted curves) and from exact calculations by Saenz et al. (red solid curves) [27]. The blue curves require no parameters except normalization. An excitation energy of 0 corresponds to a binding energy of 1.897 eV. Figure taken from [5].

3.2 Modeling Assumptions

There are three assumptions made in this work to model the capture electron energy spectrum:

- 1) Only the molecular ground state is relevant for this analysis

The FSD consists of a ground state at low E_f and excited states at higher E_f , separated by an energy gap (cf. Fig. 3.3). The ground state arises from the rotational and vibrational ("rovibrational") degrees of freedom of the molecule, while the excited states stem from electronic excitations. Assumption 2) can be justified by considering the signal over background ratio (S/B). Not only are the excited states stretched out over a larger energy range and have less excitation probability per state than the ground state, they are also separated from the ground state by more than 20 eV. This means that every excited state shifts the energy of a capture electron well below the β endpoint, where the background from β decay electrons increases massively. Fig. 3.2 shows the signal over background ratio of a simulated KATRIN integral spectrum. The simulation was performed with a relic overdensity of $\eta = 2 \cdot 10^9$, a previously obtained sensitivity limit of KATRIN [17], for the full KATRIN data set after the nominal runtime of 1000 days. The ground state peak on the right of the plot is clearly visible, reaching a S/B of almost 0.01. The excited states, on the other hand, make a difference of only $O(10^{-6})$, which would clearly not be discernible in the data.

- 2) The FSDs for β decay and neutrino capture are identical: $P_{f,\beta}(E_f) = P_{f,\text{capture}}(E_f)$

Since assumption 1) is justified, it is enough to show that the molecular ground states for β decay and neutrino capture are equal to good approximation to justify 2). The FSD ground state is one singular peak with a mean energy and a considerable width, originating from thermal motion of the

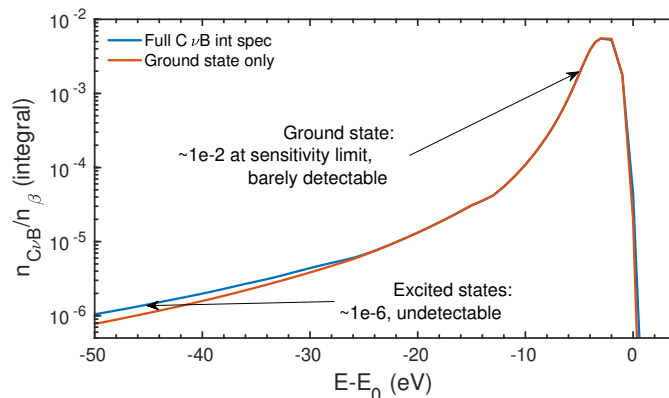


Figure 3.2: Number of capture electrons $n_{C\nu B}$ divided by the number of β electrons, n_{β} (integral), simulated at the KATRIN sensitivity limit (KATRIN nominal settings, cf. Tab. 4.2)

nuclei inside the molecule, which leads to a smearing of the total recoil energy and the energy of the outgoing electron. At low temperatures, such as in the KATRIN source which operates at 27 K, this width is dominated to 96% by the zero point motion of the nuclei, which is irreducible and arises from the initial state [5]. Therefore, the FSD effects of β decay and ν capture are the same to good approximation, since the two processes share the same initial state. Fig. 3.1 shows a comparison between the full description of the FSD ground state and the description from zero point motion only.

3) The molecular ground state may be approximated by a Gaussian.

Finally, to justify assumption 3), Monte Carlo data sets were fitted with the exact FSD ground state and with the Gaussian approximation. See Sec. 5.1 for more information on KATRIN Monte Carlo data sets. Without statistical fluctuations, the bias introduced by assumption 3) is less than one part per thousand in terms of standard deviation across all fit parameters (m_{ν}^2, E_0, N, B and η , see Sec. 3.6 for a full breakdown of all model parameters). With statistical fluctuations, the bias is still less than 5% in terms of standard deviation for all fit parameters. Fig. 3.3 illustrates the model before and after assumptions 2) and 3). The full convolution with the FSDs, already Doppler broadened, is shown in blue, with the excited states partially visible at lower energies. The Gaussian fit of the ground state is overlaid in red, showing good agreement between the two.

With the model reduced to a single Gaussian, there are only three parameters left to fully describe the signal: **position** $\langle E_{C\nu B} \rangle$, **width** $\sigma_{C\nu B}$ and **normalization** η , which will be discussed in the following sections.

3.3 Position of the Relic Neutrino Signal in the Energy Spectrum

A priori, the mean energy of a capture electron should be $2m_{\nu}$ larger than the endpoint energy of the β spectrum. However, both the relic neutrino signal and the β electrons are affected by the nuclear recoil and the FSDs

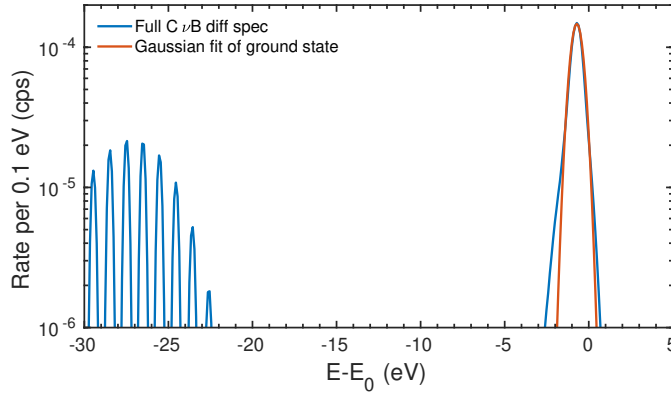


Figure 3.3: Capture electron differential spectrum before and after assumptions 2) and 3)

in different ways, which smear out this difference in the measured spectrum. The discussion of nuclear recoil and the molecular final states follows largely the semi-classical approach of [5]. Like mentioned above, the tritium atoms in the WGTS are bound in three different molecules, tritium-tritium (TT), deuterium-tritium (DT), and hydrogen-tritium (HT). For each of these molecules, there exist upper and lower bounds on the recoil energy from considering the limits of very strong and very weak molecular bonds. The recoiling mass is either the tritium nucleus only, for a weak bond, or the entire molecule in case of a strong bond. Dependent on the recoiling mass, the recoil energy can be approximated as follows:

$$E_{\text{rec}}^{\text{kin}} = Q \cdot \frac{m_e}{m_e + M_{\text{rec}}} \quad (3.3)$$

Here, Q is the total energy released in the β decay, m_e is the mass of the electron and M_{rec} is the recoiling mass. The bounds on M_{rec} and Eq. 3.3 yield upper and lower bounds on $E_{\text{rec}}^{\text{kin}}$. For the TT molecule, They are: $1.7 \text{ eV} \leq E_{\text{rec}}^{\text{kin}} \leq 3.41 \text{ eV}$ [5]. If the molecule remains bound after the β decay, 1.7 eV of the recoil energy are going into translational energy of the molecule (via conservation of momentum). This is less than the binding energy of the daughter molecule ${}^3\text{HeT}^+$ [5], so the molecule does remain bound, leaving the remaining 1.7 eV of the maximally possible 3.41 eV for internal molecular excitations, described by the FSD. As it turns out, it is a good approximation to assume that the medium energy of the molecular ground state peak is equal to those remaining 1.7 eV.

Three separate FSDs are needed, one for TT, one for DT and one for HT. Due to their different partner nuclei, the translational energies of the three molecules as well as their absolute initial and final energy levels differ, so there are effectively three different spectra with three different endpoints. This is of no great concern to the analysis, since the endpoint is a free fit parameter anyway. For convenience, these differences are incorporated in the FSDs, which is why they are given relative to the translational energy of a ${}^3\text{HeT}^+$ daughter molecule [18]. All three ground state peaks are therefore located at approximately $E_{\text{GS}}^{\text{TT}} = E_{\text{GS}} = 1.7 \text{ eV}$ on the relative energy axis.

As discussed in Sec. 3.2, and in contrast to the translational recoil energy of the molecule, the FSD ground state energy has a considerable width. As

can be seen in Fig. 3.1, there is a non-zero probability for having no rovibrational excitation at all [5], which has important consequences for the relic neutrino search. The average energy gap between a capture electron and a β electron emitted at the endpoint is still $2m_\nu$, however the endpoint is not a peak. The average energy gap offers little value for this analysis. Instead, the position of the relic neutrino peak relative to the endpoint is given by the minimally possible separation between a β decay electron and the mean of the relic neutrino peak. Since there exists a non-zero chance of having no rovibrational excitation, the maximally possible energy that is reachable by β decay electrons is, in contrast to their mean energy, effectively not impacted by ground state energy losses. The position of the relic peak on the other hand, denoting the mean energy of the neutrino capture electrons, is shifted by the full -3.4 eV of the recoil energy. Due to this difference in the nature of the relic peak position and the endpoint, the relic peak in the KATRIN data will not be two neutrino masses above the endpoint, but instead only $\Delta E = 2m_\nu - 1.7$ eV, meaning that for a neutrino mass below 0.9 eV, the relic peak is below the endpoint, significantly reducing the chances of detection. Fig. 3.4 illustrates the effects of the ground state width for a neutrino mass squared of 2 eV²: the β and $C\nu B$ energy spectra were simulated two times (for an arbitrary measurement period and η), but in one case, all final states were set to zero excitation energy relative to the ${}^3\text{HeT}^+$ recoil: $P_f(E_f) = \delta(0)$. In that case, the $C\nu B$ peak is located $2m_\nu$ above the endpoint, and only broadened by the Doppler effect. Except for a static shift by 8 eV to lower energies [5], this is how the spectrum would look like for atomic tritium. When the ground state width is introduced, the $C\nu B$ peak is broadened and shifted relative to E_0 by the ground state energy E_{GS} . E_0 is unaffected, but the β spectrum is strongly suppressed near the endpoint. Because the relic peak position depends on the neutrino mass, it is also necessary to address the possibility of a negative m_ν^2 , which is permitted by the fit model. In such a case, it is not possible to take the square root of the fitted m_ν^2 to determine the position of the relic peak. Rather, the relic peak is located where it would be if $m_\nu = 0$, i.e. 1.7 eV below the endpoint.

3.4 Differential Width of the Relic Neutrino Signal

The intrinsic energy width of the relic neutrino background is only around 1 meV, and the width of the measured relic neutrino signal is dominated by other effects. The FSD ground state contributes the largest part, with $\sigma \approx 390$ meV. Given here is the width of the Gaussian fit to the ground state, which is slightly smaller than the width of the exact FSD ground state of 440 meV. Another contribution comes from the Doppler effect, which is dependent on the kinetic energy and hence temperature of the molecules in the source, and gives another 94 meV of broadening.

3.5 Expected Rate of the Relic Neutrino Signal in KATRIN

The expected rate and hence the normalization of the relic neutrino signal is proportional to the overdensity η . To extract any useful information about

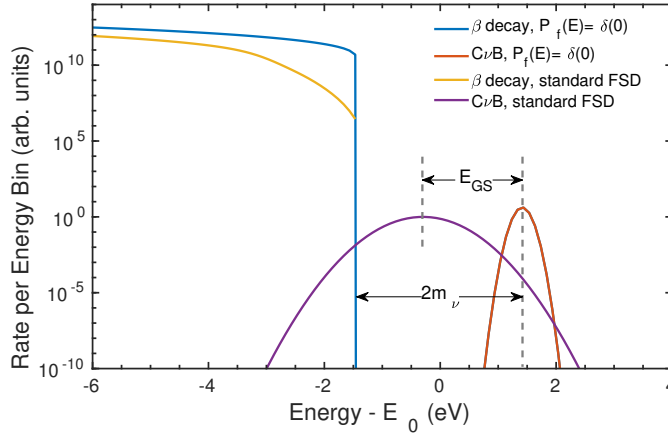


Figure 3.4: β decay endpoint and relic neutrino peak for a neutrino mass squared of 2 eV^2 , for normal FSD and for the case $P_f = \delta(0)$. The ground state significantly broadens the relic peak and shifts it towards the endpoint. It also leads to a suppression of the rate near the endpoint of the β spectrum.

η , precise knowledge about the expected capture electron rate at the KATRIN detector given a certain overdensity is crucial. This rate is dependent on the KATRIN specifications of the measurement campaign, for example the amount of tritium in the source or the magnetic fields, and has to be calculated for every data set individually.

3.5.1 Total Rate of Relic Neutrino Captures in the WGTS

Starting from R_ν derived in Sec. 3.1, the capture rate inside the KATRIN source is derived by multiplying the rate per atom, R_ν , with the number of tritium atoms in the KATRIN source, as stated in Eq. 3.4.

$$R_\nu^{\text{WGTS}} = R_\nu \cdot 2 \cdot \rho_d \cdot \pi \cdot r_{\text{beamtube}}^2 \cdot \epsilon_T \quad (3.4)$$

Here, ρ_d denotes the column density of molecules per square centimeter in the source, r_{beamtube} is the radius of the Windowless Gaseous Tritium Source (WGTS) beam tube and ϵ_T is the tritium purity. The experimentally measurable rate in KATRIN is not equal to R_ν^{WGTS} due to the experimental response as well as the FSD excited states (cf. Sec. 3.5.2). All these losses will be accounted for below using KATRIN design report quantities for illustration.

3.5.2 FSD Losses

As discussed in Sec. 3.2, the excited states, which make up about 43% of the total FSD, can be neglected to estimate the useful capture rate. Thus, the fraction ϵ_{FSD} of electrons in the ground state, which is equal to 57%, is applied to the normalization of the expected signal.

3.5.3 Zero Scattering Probability

Since KATRIN is measuring an integral spectrum, it measures all the electrons over a certain energy threshold set by a retarding potential (or retarding energy). The region of interest for relic neutrinos is around or slightly above the endpoint, at high retarding potentials. Electrons loose 10 eV from a single inelastic scattering event [7]. Therefore, for the same reason that the FSD excited states can be neglected, electrons from capture reactions that scatter inelastically only once inside the source can be neglected as well. At nominal column density, the probability P of an electron not scattering once before it leaves the source is 42% [7].

3.5.4 Acceptance Angle of the Spectrometer

The capture electrons are released isotropically, but KATRIN can only measure electrons up to a solid angle Ω . This solid angle depends on the largest angle θ_{\max} at which an electron can be emitted in the WGTS and still reach the detector, which in turn depends on the source and pinch magnetic fields, B_S and B_{\max} . For the purpose of the evaluation presented in this section, the values from the KATRIN technical design report are used, $B_S = 3.6\text{ T}$ and $B_{\max} = 6\text{ T}$ [7]. With this, Ω and θ_{\max} are calculated using Eq. 3.5 and 3.6:

$$\theta_{\max} = \text{asin}\left(\sqrt{\frac{B_S}{B_{\max}}}\right) = 0.8861 \quad (3.5)$$

$$\frac{\Omega}{4\pi} = \frac{1}{2}(1 - \cos(\theta_{\max})) = \epsilon_{\text{acceptance}} = 0.184 \quad (3.6)$$

3.5.5 Detector Effects

ϵ_{FPD} is the probability of an electron being detected if it reaches the end of the spectrometer. If an electron is emitted inside the angle of acceptance, it is almost guaranteed to hit the detector which has a coverage of 99.9%. However, depending on the run period, there might be some inactive pixels (e.g. KNM1: only 79% of pixels have been considered for the analysis). The detector itself has an absolute efficiency for detecting electrons of about 18 keV, taken to be 95%.

3.5.6 Effective Tritium Mass and Expected Rate

The usual definition for the effective tritium mass in KATRIN given in the literature only takes into account the acceptance angle and zero scattering probability [17][8], since the detector effects absent any inactive pixels are essentially one and the final states are not as relevant for the beta decay electrons. For this analysis, the final state losses are quite relevant (cf. 3.5.2), so a different definition makes sense that takes the FSD losses ϵ_{FSD} into account as well. Using the maximum column density from the design report of 5×10^{17} molecules/cm² and a beamtube radius of 4.11 cm [7], the effective tritium mass is:

$$m_{\text{eff}} = m_{\text{TT}} \cdot 5 \cdot 10^{17} \frac{1}{\text{cm}^2} \cdot \pi \cdot r_{\text{beamtube}}^2 \cdot \epsilon_{\text{acceptance}} \cdot \epsilon_{\text{FSD}} \cdot P = 11.1 \mu\text{g} \quad (3.7)$$

Effect	Fraction of surviving e^-
angle of acceptance	0.184
detector efficiency	0.95
detector coverage	0.999
inactive pixels	1
excited states	0.57
zero scattering	0.42
all effects combined	0.042

Table 3.1: Experimental yields for KATRIN nominal settings
(cf. Tab. 4.2)

And for the capture rate, one gets:

$$R_\nu^{\text{exp}} = R_\nu^{\text{WGTS}} \cdot \epsilon_{\text{acceptance}} \cdot \epsilon_{\text{FPD}} \cdot \epsilon_{\text{FSD}} \cdot P \approx 1.6 \times 10^{-6} \text{ yr}^{-1} \quad (3.8)$$

Using the KATRIN specifications from the design report, an estimated $4.3 \cdot 10^{-6}$ counts without overdensity occur over the total projected measurement time for KATRIN of 1000 days.

3.6 Fit Model Including a Relic Neutrino Signal

The fit model is the standard integral spectrum used in the KNM analyses, plus an additional term for the relic neutrinos. The differential spectrum looks like:

$$\frac{d\Gamma}{dE} = \left(\frac{d\Gamma}{dE} \right)_\beta + \left(\frac{d\Gamma}{dE} \right)_{\text{C}\nu\text{B}} \quad (3.9)$$

The first term is derived from Fermi Theory and the final state distribution:

$$\begin{aligned} \left(\frac{d\Gamma}{dE} \right)_{\beta, \text{M}} &= C \cdot F(Z, E) \cdot p \cdot (E + m_e) \\ &\cdot \sum_f P_{f, \text{M}} \cdot (E_0^{f, \text{M}} - E) \cdot \sqrt{(E_0^{f, \text{M}} - E)^2 - m_\nu^2} \cdot \Theta(E_0^{f, \text{M}} - E - m_\nu) \end{aligned} \quad (3.10)$$

$$\left(\frac{d\Gamma}{dE} \right)_\beta = N \cdot \sum_{M=\text{TT}, \text{DT}, \text{HT}} N_{\text{T}} \epsilon_{\text{M}} \cdot \left(\frac{d\Gamma}{dE} \right)_{\beta, \text{M}} \quad (3.11)$$

with a constant C containing the Fermi constant, the Cabibbo angle and the nuclear matrix element, the Fermi function $F(Z, E)$ dependent on the electron energy E and the atomic number of the daughter nucleus Z, the electron momentum p and a Heavyside function for energy conservation. Each final state f of each molecule M has an associated endpoint that is lowered by the excitation energy $E_{f, \text{M}}$ of that final state: $E_0^{f, \text{M}} = E_0 - E_{f, \text{M}}$. Each of these final states is weighted with its associated excitation probability $P_{f, \text{M}}$ and summed over. The endpoint E_0 and the neutrino mass square m_ν^2 are free parameters. This is done for the three molecules TT, DT and HT. The three spectra are subsequently summed together according to Eq. 3.11, weighted by the molecular fractions ϵ_{M} . N_{T} equals 2 if M=TT, and 1 otherwise, to account for the TT molecule containing twice as much tritium as

the other two. N is the signal normalization factor of the β spectrum, another free fit parameter.

For the relic neutrino signal, a single Gaussian peak is used to describe the differential spectrum. Its position relative to the endpoint of the β spectrum is $\Delta E = 2m_\nu - \langle E_{\text{FSD,ground}} \rangle$, with $\langle E_{\text{FSD,ground}} \rangle = 1.7$ eV, as discussed in Sec. 3.3. Its width is determined by the width of the molecular ground state and the Doppler effect broadening due to thermal motion of the molecules in the WGTS. The FSD ground state has a width of 440 meV, which is slightly larger than the width of the Gaussian fit that is used to approximate the relic neutrino differential spectrum. The Doppler effect only contributes 93.5 meV, leading to a total width of $\sigma_{\text{C}\nu\text{B}} = 400$ meV. The normalization is derived from the capture rate in the WGTS, R_ν^{WGTS} as discussed in Sec. 3.5 by taking into account signal losses that occur between source and detection. These include the acceptance angle of the spectrometer, detector efficiency and coverage, the FSD excited states probability, but not the zero scattering probability P , which is included in the response function. The relic term is then:

$$\left(\frac{d\Gamma}{dE} \right)_{\text{C}\nu\text{B}} = \frac{\eta \cdot R_\nu^{\text{exp}} \cdot T}{P \cdot \sqrt{2\pi\sigma_{\text{C}\nu\text{B}}^2}} \cdot \exp\left(-\frac{(E - E_0 - 2m_\nu + \langle E_{\text{FSD,ground}} \rangle)^2}{2\sigma_{\text{C}\nu\text{B}}^2} \right) \quad (3.12)$$

with T being the total measurement time and the relic neutrino width $\sigma_{\text{C}\nu\text{B}}$ determined from the FSD ground state width and the Doppler effect broadening. The relic neutrino overdensity η appears as another free parameter. The integral spectrum is subsequently derived using the response function R , which relates the transmission probability of an electron to its energy and the retarding potential qU of the spectrometer. R is derived by folding the energy loss distribution of electrons in the source with the transmission function of the spectrometer [7]. A full derivation can be found in [7]. The integral spectrum is then:

$$S(qU) = \int_{qU}^{E_0} \frac{d\Gamma}{dE}(E) \cdot R(E, qU) dE + B \quad (3.13)$$

From this one gets the last free parameter, the energy-independent background rate B . In total there are five free fit parameters in the model: the endpoint E_0 , the neutrino mass square m_ν^2 , the relic neutrino overdensity η , the signal normalization N and the background rate B . Fig. 3.5 shows a simulation of the model described above. In this case, the KATRIN design report settings were used. The top panel shows both a simulation with a relic neutrino signal at the sensitivity limit ($\eta = 2.8 \times 10^9$) and a model with no relic signal. Viewed like this, the difference between the two cannot be spotted by eye. In the middle panel, the signal over background ratio of the relic neutrino signal is depicted. Here the difference is clearly visible. Both the top and middle panel include the fit parameters of the model, with arrows next to them indicating the deformation in the graph that is caused by a change of the parameter value. The bottom panel shows the design report measurement time distribution (MTD).

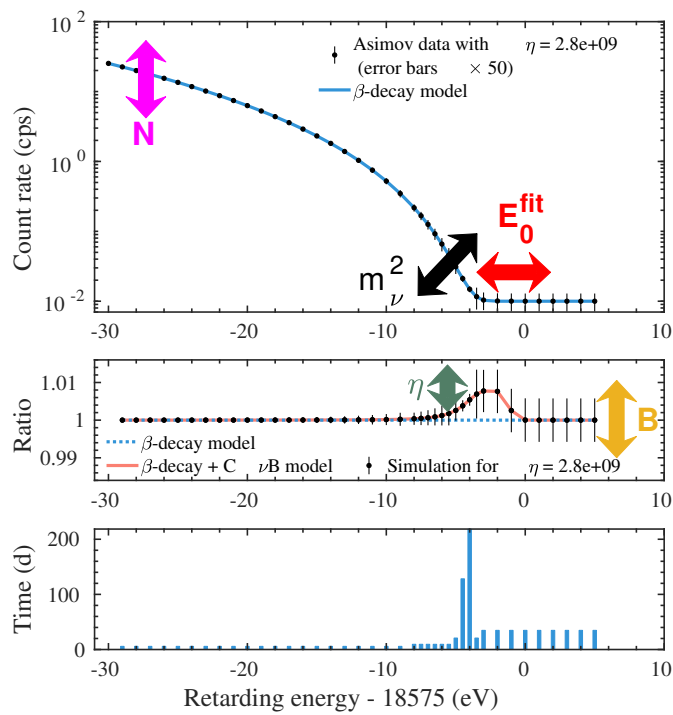


Figure 3.5: Simulation of a KATRIN integral spectrum (design report settings) with a relic neutrino signal at the sensitivity limit. The fit parameters and their impact on the shape of the spectrum are shown as well.

Chapter 4

Data Sets

4.1 KRN1 Measurement Campaign

4.1.1 KRN1 Configuration

For this relic neutrino analysis (KATRIN Relic Neutrino 1, or KRN1), twin Monte-Carlo copies of the first high-purity tritium measurement campaign of the KATRIN experiment were used, which ran from April 10 to May 13, 2019. The total measurement time clocks in at just under 23.4 days, divided into 274 runs. This campaign was conducted at an average column density of $\rho d_{\text{exp}} = 1.11 \cdot 10^{17}$, which is a fifth of the nominal value, and an average tritium purity of $\epsilon_{\text{T}} = 0.976$. The magnetic field settings deviated from the design values: $B_{\text{S}} = 2.51 \text{ T}$ and $B_{\text{max}} = 4.23 \text{ T}$. Additionally, there were 31 detector pixels that were too noisy or shadowed by instruments in the beamline and had to be excluded. The integral β spectrum was scanned over an energy range of $[E_0 - 90 \text{ eV}, E_0 + 40 \text{ eV}]$, however at the time of this work, only parts of this energy range were available for analyses beyond the neutrino mass. This is due to the unblinding protocol of the KATRIN collaboration that requires a blind neutrino mass analysis (using a distorted FSD) of several independent groups before fitting any unblinded KATRIN data. The energy range from 40 eV below to 50 eV above the endpoint was used in the KNM1 analysis and is therefore already unblinded [3], which is why the same energy range was used in this work as well.

4.1.2 KRN1 Expected Rate

Tab. 4.1 summarizes the experimental response during the KNM1 measurement campaign. Note that the zero scattering probability is higher due to the lower column density. The effective tritium mass for KRN1 is $5.5 \mu\text{g}$, and therefore one has an expected relic neutrino capture count of $4.0 \cdot 10^{-8} \cdot \eta$.

4.2 KATRIN Design Monte Carlo Data Set

To calculate an expected sensitivity limit for the KATRIN experiment, an Asimov data set (not statistically fluctuated, cf. Sec. 5.1) simulating the entire projected run time of KATRIN was generated. The KATRIN experiment plans to collect data for 1000 days in total at its nominal column density of $5 \times 10^{17} \text{ molecules/cm}^2$ with a tritium purity of 97%. The expected neutrino capture count is $4.3 \cdot 10^{-6} \cdot \eta$ (for a detailed derivation of this number, see Sec. 3.5). Tab. 4.2 summarizes the differences between KRN1 and KATRIN

Effect	Fraction of surviving e^-
angle of acceptance	0.182
detector efficiency	0.95
detector coverage	0.999
inactive pixels	0.79
excited states	0.57
zero scattering	0.79
all effects combined	0.065

Table 4.1: Experimental yields in KATRIN for KRN1

nominal. Note that the beam tube radius for KATRIN nominal is smaller than the physical radius of the WGTS of 4.5 cm. This is due to the higher source magnetic field B_S creating an effective flux tube that is smaller than the WGTS. These settings have mostly been taken from the KATRIN design report [7], with the exception of the background rate, which was estimated to be only 10 mcps in [7]. This proved to be unrealistic in practice due to unexpected, non-Poissonian background contributions from radon and wall decays in the spectrometer. In this work, an updated estimate of 130 mcps across all pixels is used instead, which is roughly equal to the current background levels seen at KATRIN as of 2020 [1]. Fig. 4.1 shows the measure-

	KRN1	KATRIN nominal
ρ_d	1.11×10^{17} molecules/cm ²	5×10^{17} molecules/cm ²
ϵ_T	0.976	0.973
B_S	2.52 T	3.6 T
B_{\max}	4.23 T	6 T
B_{ana}	6.3112×10^{-4} T	3×10^{-4} T
fraction of inactive pixels	0.79	1
r_{beamtube}	4.5 cm	4.11 cm
background rate	293 mcps	130 mcps
measurement time	23.4 days	1000 days

Table 4.2: Settings for KRN1 and KATRIN nominal simulations

ment time distributions (MTDs) of the two MC data sets. The KRN1 MTD was adapted significantly from the design report one, dedicating more time to background measurement and measuring to higher energies to search for a possible background slope.

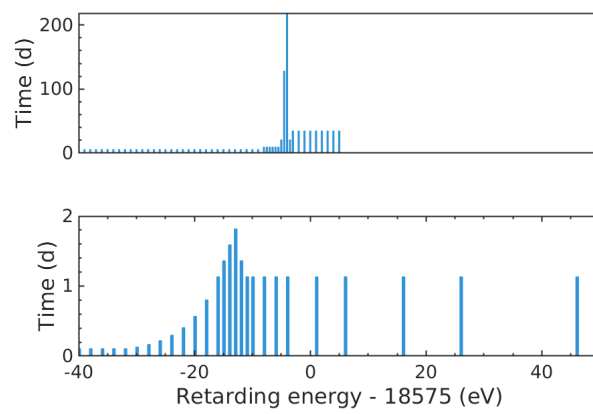


Figure 4.1: MTDs of KATRIN nominal (top) and KRN1 (bottom)

Chapter 5

Analysis on Monte Carlo Simulations

5.1 KRN1 Monte Carlo Data Sets

There are two types of Monte Carlo (MC) data used in this work: Asimov and fluctuated. An Asimov MC data set is a straightforward prediction of the expected rate measured by the KATRIN detector at each HV set point, performed for each individual run and then stacked together. The resulting spectrum is the expected average outcome of the measurement campaign. The true outcome however will include random fluctuations, both from statistical and systematic effects. If these random fluctuations are added, the MC is referred to as ‘fluctuated’ and represents one possible outcome of the measurement campaign. An MC generated to match an existing data set is called ‘twin’. In this sense, KRN1 twins are MC data sets that mimic the KRN1 data set described in Sec. 4.1. On the other hand, MCs that do not have a matching existing measurement campaign, no matter if they are Asimov or fluctuated, are called ‘fake’. The KATRIN design MC (Sec. 4.2) falls into this category.

5.1.1 Sensitivity Estimation of KRN1 Using Asimov Twins with Different True Neutrino Masses

To determine the sensitivity on the relic neutrino overdensity, a β decay spectrum plus relic term is fitted to unfluctuated KRN1 twins with a true relic neutrino overdensity of zero (The expected overdensity around Earth is zero to good approximation compared to the KATRIN sensitivity, cf. Sec. 1.2). The four fit parameters E_0 , N , B and m_ν , are treated as nuisance parameters, while η is varied to calculate its χ^2 profile. For Asimov twins, a fit with $\eta = 0$ can reproduce the twin data almost perfectly, with $\chi^2 \approx 1 \times 10^{-3}$. The normalization of the relic peak is increased until the χ^2 of the fit has grown by 2.71 with respect to the best fit value, which corresponds to the 90% sensitivity on the relic peak normalization and hence on the overdensity η [32]. Fig. 5.1 illustrates this for an Asimov MC with a true neutrino mass of 0 eV. Since the neutrino mass is still unknown, this has to be done for a sensible range of possible neutrino masses. To this end, different twin data sets with different true neutrino mass values (hereinafter referred to as ‘true neutrino mass’) were used. This method can be used to investigate the effect of a ‘known’ neutrino mass value on the relic neutrino limit, and is a good benchmark to compare to earlier studies. Fig. 5.2 displays the KRN1 sensitivity for Asimov twins vs. the true neutrino mass. In a mass range

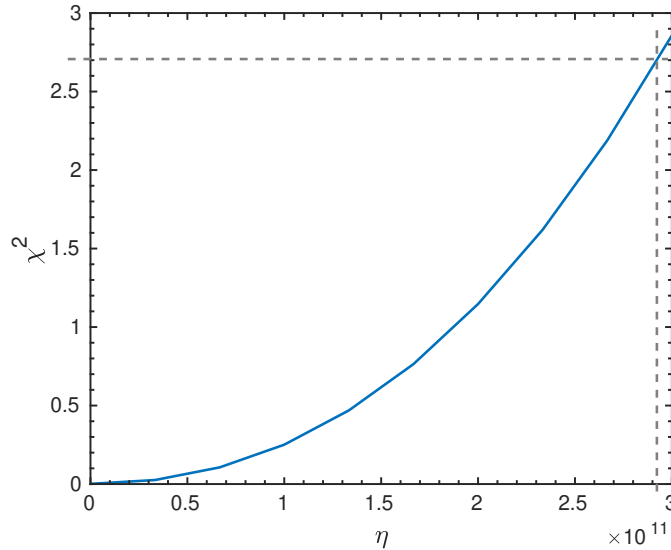


Figure 5.1: χ^2 profile of the overdensity of relic neutrinos for a true neutrino mass of 0. The dashed lines denote a $\Delta\chi^2$ of 2.71 and the corresponding 90% limit on η .

between 0 and 2 eV, the 90% sensitivity of KRN1 ranges from 2.9×10^{11} to 2.2×10^{11} , improving with growing true neutrino mass. This relation has been found in earlier studies as well, such as [17] and can be explained by the growing separation between endpoint and relic peak for larger neutrino masses. The KRN1 sensitivity, shown in Fig. 5.2 surpasses both the limits reported by the Los Alamos [26] and Troitsk [21] collaborations, as well as the cosmic ray limit derived by [14] by more than an order of magnitude. Fig. 5.2 also includes the KATRIN sensitivity limit from an earlier study by Kaboth et al. [17], representing the best case scenario in which the targeted KATRIN background rate of 10 mcps would have been reached. All other lines and areas in Fig. 5.2 are theoretical predictions from various models.

5.1.2 Sensitivity Estimation of KRN1 with Fluctuated Twins

To verify the robustness and stability of the fit model, 1000 fits were performed on a KRN1 twin data set with added statistical and systematic fluctuations. The true overdensity as well as the true neutrino mass were both zero. The fit parameters are m_ν^2 , E_0 , normalization, background and η . With the fluctuations, the typical χ^2 of the fit increased from zero to a mean of 22, following the expected χ^2 distribution with 22 degrees of freedom. The best fit value of η is strongly driven by the fluctuations in the vicinity of the neutrino capture peak. Fig. 5.3 shows an exemplary fit to a typical fluctuated spectrum with a mid-range η best fit value to illustrate how the relic peak follows the random fluctuations. Fig. 5.4 shows the distribution of the best fit values of η . Negative η values are statistically allowed, but unphysical. With a median of -1.6×10^{10} (a bias of 0.08 in unit of standard deviation) and a standard deviation of 1.9×10^{11} , the true value could be reproduced within the uncertainty. One can also derive an estimate of the 90% sensitivity of KRN1 by multiplying the standard deviation by 1.645, yielding 3.1×10^{11} , which agrees reasonably well with the values obtained by χ^2 scans. Due to the high computational demand of calculating 1000 fits

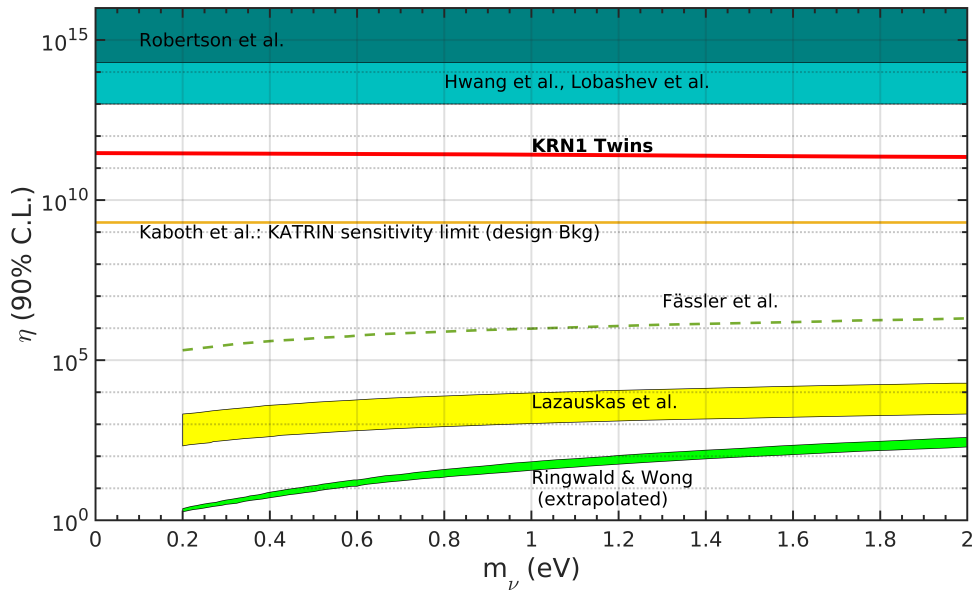


Figure 5.2: η sensitivity of KRN1 twins with different true neutrino masses. Other limits and predictions taken from Robertson et al. [26], Hwang et al. [14], Lobashev et al. [21], Kaboth et al. [17], Fässler et al. [10], Lazauskas et al. [20] and Ringwald/Wong [25].

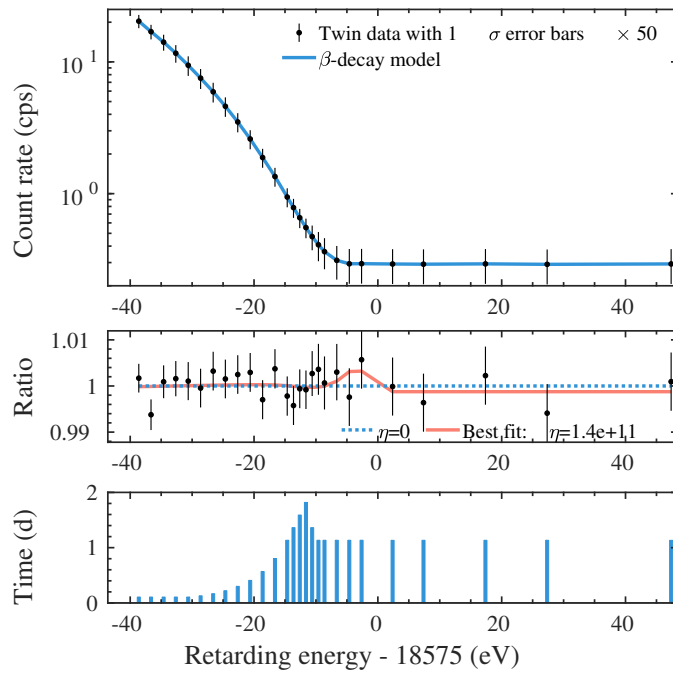


Figure 5.3: Example fit with random fluctuations added. True $\eta = 0$.

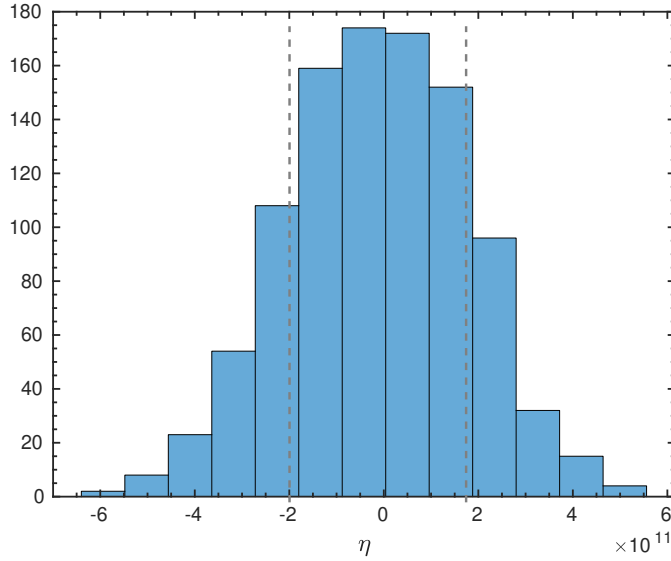


Figure 5.4: Distribution of the best fit values of the overdensity after 1000 fits of KRN1 twins with random statistical fluctuations added. The true η value of zero is reproduced within uncertainty. Grey lines indicate 1 standard deviation from the mean.

with 5 free parameters, this sensitivity estimation was only done for one neutrino mass, $m_\nu = 0$ eV.

5.1.3 Systematics Breakdown Using KRN1 Twins

Systematic uncertainties are propagated using covariance matrices. The systematic effects relevant for this analysis are:

The final state distribution: contains the shape uncertainty (uncorrelated uncertainty of each bin) and uncertainty on the relative normalization of ground state and excited states,

Fluctuations in the tritium activity between runs: hereinafter referred to as 'scan fluctuations',

Detector efficiency,

Theoretical corrections: mainly radiative corrections,

The response function: uncertainties on the the magnetic fields in the source (B_S) and spectrometer (B_{\max}, B_{ana}), the column density and inelastic scattering cross section all factor in here,

The background slope: accounts for a possible linear energy dependence of the background,

The background rate: originates from an unexpected non-Poissonian factor in the background rate distribution,

Stacking: due to differences in the spectrometer high voltage from run to run.

Tab. 5.1 lists the systematic uncertainties associated with each effect.

Parameter	uncertainty (relative unless stated otherwise)
FSD normalization	0.01
FSD GS shape	0.04
FSD ES shape	0.18
B_{ana}	0.01
B_{max}	0.002
B_{S}	0.025
ρ_{d}	0.0085
Scan fluctuations	5×10^{-4}
Theoretical corrections	2×10^{-4}
Detector efficiency	1×10^{-4}
Background slope	5.2×10^{-6} cps/eV
Non-Poissonian factor	1.064

Table 5.1: Systematics budget for KRN1

The systematics breakdown of η was calculated for a true neutrino mass of 1 eV^2 , using only individual covariance matrices to propagate the uncertainties. First the sensitivity was determined taking all systematics into account, yielding the total limit η_{tot} at 1σ C.L. Next, for each systematic effect i , only the respective systematic uncertainty was taken into account and the sensitivity was determined again, yielding η_i (again, at 1σ C.L.). The individual contribution of the i -th systematic effect is then $\Delta_i = \sqrt{\eta_{\text{tot}}^2 - \eta_i^2}$. The uncertainties in the KRN1 analysis are statistics dominated, with the total systematic variance making up less than 15% of the total variance (not considering a combination in quadrature, at this stage). The dominant systematic uncertainty is due to the non-Poissonian background rate, similar to the KNM1 analysis. The contribution of the background rate is a factor of 5 larger than the next largest systematic effect. Investigations for different true neutrino masses show that the dominance of background related systematics is increasing for larger true neutrino masses for which the relic peak is separated more from the endpoint. Results are displayed in Fig. 5.5 and Tab. 5.2. It should be noted that there are systematic uncertainties that were neglected during the data taking of KRN1, mainly originating from plasma effects in the WGTS and from the Penning trap between pre- and main spectrometer. These uncertainties were subsequently shown to have an effect of around 20% on the KNM1 neutrino mass. As outlined in Sec. 4.1.1, a prerequisite of this analysis is a rigorous, blind neutrino mass analysis with the same settings and data set. As of this work, there was no such neutrino mass analysis that included the new systematic effects, so they were excluded here as well. However, with the relic neutrino signal heavily statistics dominated, such effects are not expected to influence the results of this analysis in a non-negligible way.

Effect	η uncertainty Cov. matrix
Statistical	1.5×10^{11}
Background rate	5.4×10^{10}
Detector efficiency	9.8×10^9
Stacking	8×10^9
Response Function	7.8×10^9
Scan fluctuations	5.4×10^9
Theoretical corrections	5.1×10^9
Final-state distribution	4.8×10^9
Background slope	2.8×10^9

Table 5.2: Systematics for KRN1 Asimov twins with a true neutrino mass of 1 eV^2

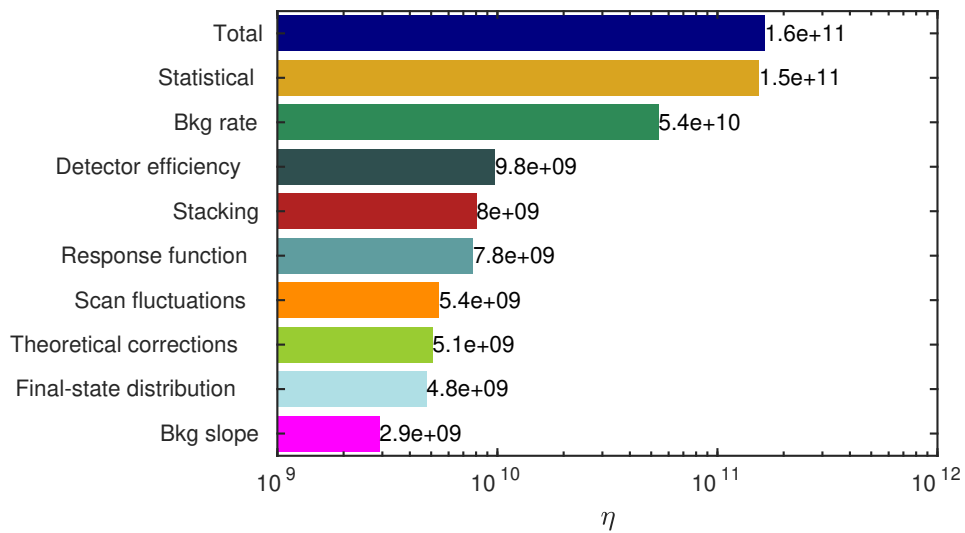


Figure 5.5: Systematics breakdown of KRN1 Asimov twins with a true neutrino mass of 1 eV^2

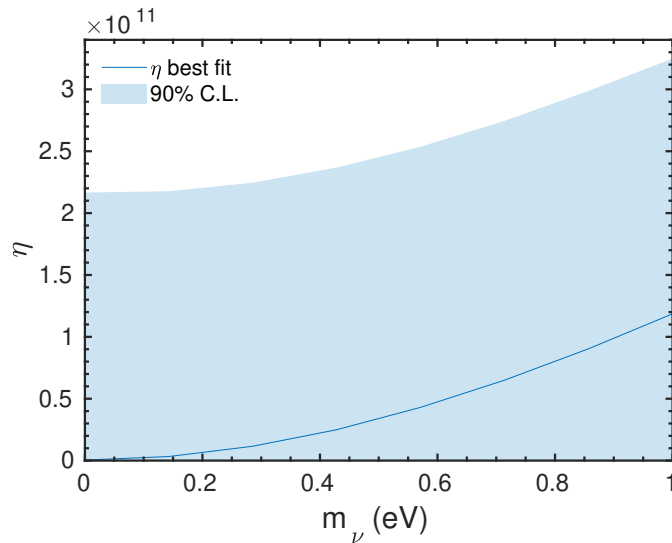


Figure 5.6: Raster scan of KRN1 Asimov MC with true $m_\nu^2 = 0 \text{ eV}^2$, showing the η best fit with 90% upper confidence bound vs. fixed neutrino mass.

5.1.4 Prediction of the Exclusion Limit: Raster Scan Method

On the data, it is not possible to set a true neutrino mass as described for the twins in Sec. 5.1.1. Instead, a scan over a sensible neutrino mass range has to be done. There are two possibilities to consider: the first option is to perform a raster scan, varying the neutrino mass between zero and 1 eV, which corresponds roughly to the 90% upper limit on the neutrino mass from the KNM1 analysis. For each of the neutrino mass scan points, the 90% confidence limit of η is determined while keeping the other nuisance Parameters E_0^{fit} , normalization and background free. To test this, an Asimov twin data set with a true neutrino mass squared of 0 eV^2 has been generated to simulate the KRN1 data set. Fig. 5.6 shows the results. For large fixed neutrino masses, the best fit value of η becomes quite large as well. This is due to an excess of rate near the endpoint of the twins with respect to the fit model if the neutrino mass is fixed to positive values. This excess of rate can be fitted by a relic neutrino signal. This effect is expected to be even more pronounced on the real data, since the best fit value of the neutrino mass squared from the KNM1 analysis is equal to -1 eV^2 , indicating an excess of rate near the endpoint from statistical fluctuations. For data, the raster scan could also suffer from the lookelsewhere effect, although a discovery with KATRIN data is unlikely. For an upper limit, this can be neglected.

5.1.5 Prediction of the Exclusion Limit: 2D Scan

The other option is to perform a 2D scan over the (m_ν, η) grid. Here, both m_ν and η are varied simultaneously around their global best fit values. At each grid point, a new fit is performed over the remaining nuisance parameters endpoint, normalization and background. From this, contours of equal $\Delta\chi^2$ can be drawn around the global best fit, providing an excluded region in the (m_ν, η) parameter space rather than a limit on η dependent on an assumed value of the neutrino mass. Fig. 5.7 shows the excluded region

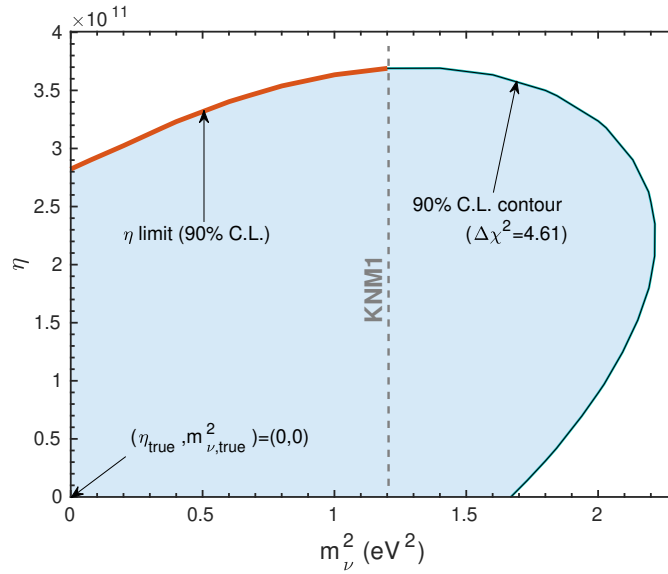


Figure 5.7: 2D scan over m_ν^2 and η using KRN1 Asimov twins with a true neutrino mass of 0 eV^2 . Includes limit on m_ν from the KNM1 analysis [3].

on KRN1 twins with a true neutrino mass of 0 eV^2 and a true overdensity of zero. A 90% confidence region as shown in Fig. 5.7 corresponds to a $\Delta\chi^2$ of 4.61 relative to the global minimum [32].

5.2 KATRIN Design Monte Carlo Data Set

The KATRIN design MC used in this analysis is generated with the specifications detailed in Sec. 4.2, with the updated background rate of 130 mcps across all pixels.

5.2.1 Reevaluation of the KATRIN Final Sensitivity Limit

With the enlarged background, the KATRIN sensitivity limit on η was found to be around 1×10^{10} for $0 \text{ eV} \leq m_\nu \leq 2 \text{ eV}$, with similar neutrino mass dependence as for the KRN1 twins. This is a little under one order of magnitude worse than the previous sensitivity limit of $\eta \leq 2 \times 10^9$ derived by Kaboth et al. [17].

5.2.2 Systematics Breakdown Using KATRIN Design MC

The systematics breakdown of the KATRIN design fake MC was calculated in the same way as for the KRN1 twins, at 1σ C.L. The systematics budget is given in Tab. 5.3. There are no systematic uncertainties on the detector efficiency and the non-Poissonian factor in the fake MC. Fig. 5.9 shows the propagated uncertainties on η for the KATRIN nominal fake MC. The uncertainty is again statistics dominated, with the largest contributing systematic uncertainty originating from the background slope. The propagated effect on the relic neutrino overdensity is zero for the background rate and the detector efficiency, as expected. The systematic uncertainty due to scan fluctuations is too small to include.

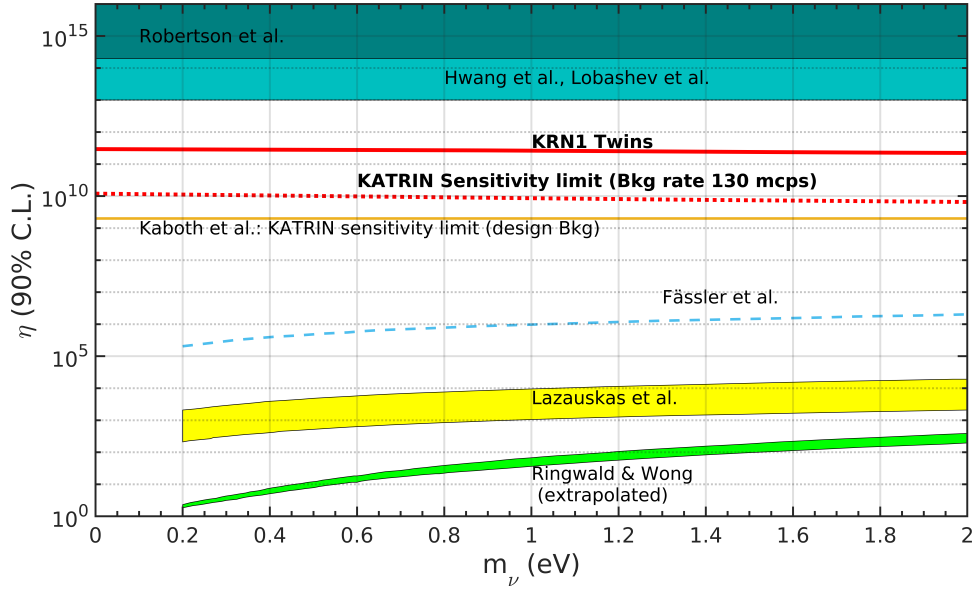


Figure 5.8: η sensitivity of KATRIN design MC with different true neutrino masses. Other limits and predictions taken from Robertson et al. [26], Hwang et al. [14], Lobashev et al. [21], Kaboth et al. [17], Fässler et al. [10], Lazauskas et al. [20] and Ringwald/Wong [25].

Parameter	uncertainty (relative unless stated otherwise)
FSD normalization	0.01
FSD GS shape	0.04
FSD ES shape	0.18
B_{ana}	0.002
B_{max}	0.002
B_{S}	0.002
ρ_{d}	0.001
Scan fluctuations	3×10^{-6}
Theoretical corrections	2×10^{-4}
Detector efficiency	0
Background slope	5×10^{-7} cps/eV
Non-Poissonian factor	1

Table 5.3: Systematics budget for the KATRIN nominal MC [7]

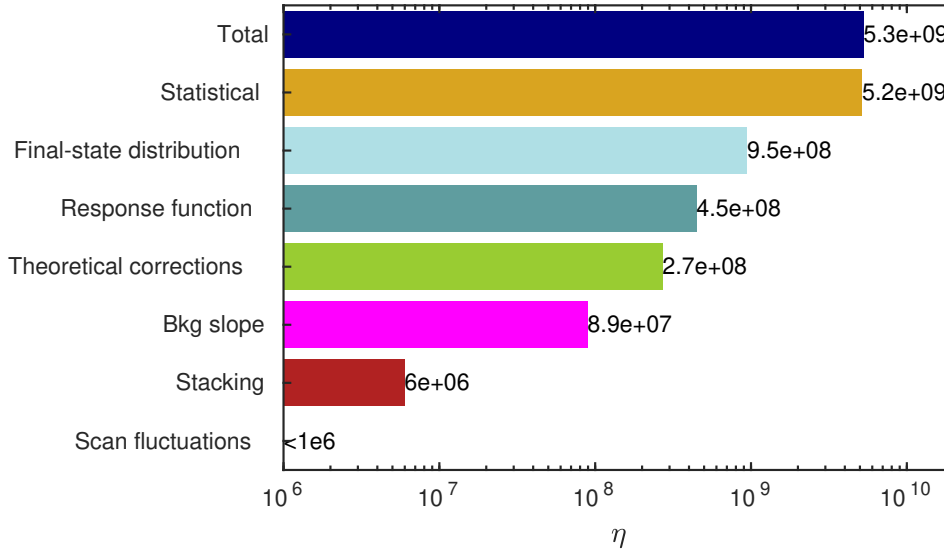


Figure 5.9: Systematics breakdown of KATRIN nominal fake MC data with a true neutrino mass of 1 eV^2

5.3 Possible Optimizations

5.3.1 MTD

The measurement time distribution (MTD) of KATRIN maximizes the neutrino mass sensitivity. However it is possible to assign more time in the energy window of the relic neutrino peak without greatly impacting the neutrino mass analysis. One such possibility for KRN1 is shown in Fig. 5.10a. Here, all existing HV set points in the background region were moved towards the relic peak window, except the last one, to keep the sensitivity to a possible HV-dependent background. Vertical dashed lines indicate the mean of the relic peak for a neutrino mass of 0 eV and 2 eV on the high end. The window of concentrated HV set points extends above and below the dashed lines by more than one standard deviation of the relic neutrino peak. Note that no measurement time is taken away from the endpoint region which could affect the neutrino mass sensitivity. Fig. 5.10b shows the sensitivity of KRN1 with the actual MTD and the proposed optimized one. The improvement is largest for small true neutrino masses, but ranges only between 3 and 10%. From this, it seems questionable to implement such an MTD, given the small benefit and the potential negative impact on the already substantial background uncertainties.

5.3.2 Atomic Tritium

Using atomic tritium for the relic neutrino search has the benefit of a narrower peak that is also more clearly separated from the endpoint (cf. 3.3). The upcoming Project 8 experiment plans on using an atomic tritium source for neutrino mass measurements, which could also be used to set a limit on the local relic neutrino overdensity [4]. A full sensitivity study on η with Project 8 is not the objective of this work. Instead, the sensitivity of KRN1 was calculated again, for a hypothetical scenario in which the molecular tritium source was replaced by an atomic one of equal intensity and 100%

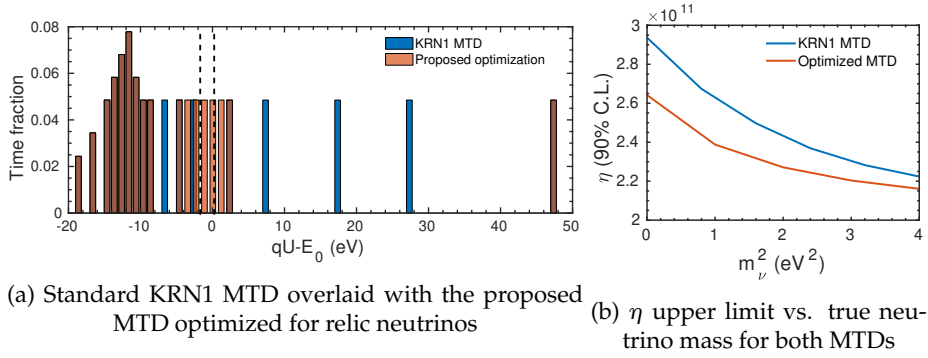


Figure 5.10: Proposed MTD optimization, compatible with neutrino mass measurements

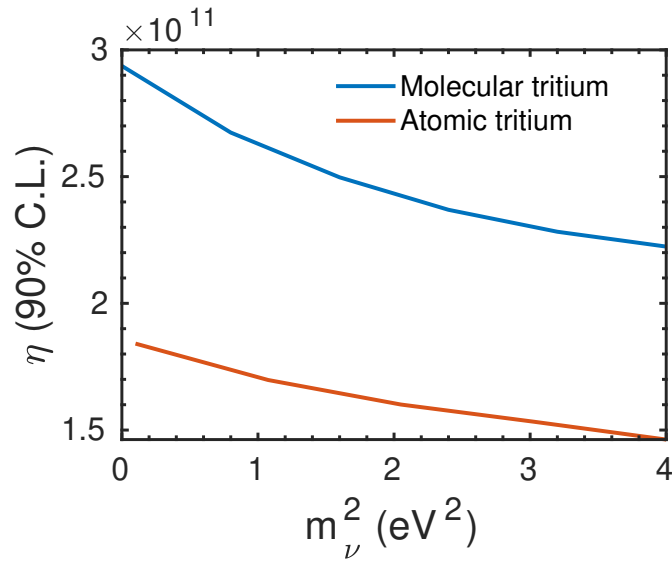


Figure 5.11: η upper limit vs. true neutrino mass if KRN1 had a 100% pure atomic tritium source.

purity. To achieve this, the FSDs were replaced by a δ function at zero excitation energy, as depicted in Fig. 3.4. The static endpoint shift between molecular and atomic tritium is of no concern to the η limit. The results, displayed in Fig. 5.11, show an improvement of the sensitivity by approximately 40%, independent of the neutrino mass. This is by its nature a very qualitative result, however it can be expected that an experiment like Project 8 would be able to surpass limits on η set by KATRIN if it achieves at least comparable amounts of statistics.

5.3.3 Theoretical Limit of a KATRIN-Type Experiment

In this hypothetical scenario, KATRIN is redesigned entirely around the search for relic neutrinos, with no regard for the neutrino mass. It still keeps a data taking time of 1000 days in total and the same source intensity, but there are three optimizations considered: An MTD concentrated exclusively around the relic peak and background regions in the energy window $[E_0 - 10 \text{ eV}, E_0 + 50 \text{ eV}]$, an atomic tritium source as described in Sec. 5.3.2, and a lowered background rate equal to the one originally aimed

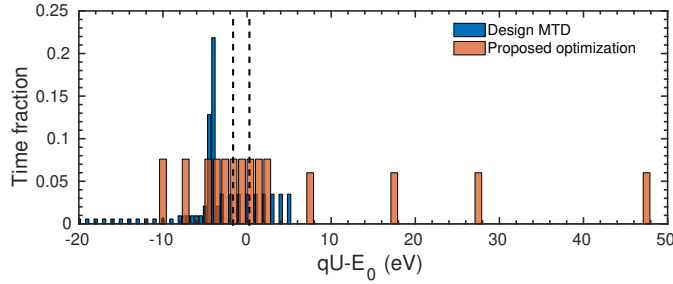


Figure 5.12: KATRIN design MTD overlaid with a proposed MTD focused exclusively on the relic neutrino search. The region of interest of the relic neutrino peak for neutrino masses between 0 and 2 eV is indicated by vertical dashed lines.

for in the KATRIN design report (10 mcps [7]). Four new η limits have been calculated, one for each optimization individually and one for all three combined. The optimized design MTD is shown in Fig. 5.12, and the resulting η limits at 90% C.L. are contained in Tab. 5.4, calculated for a true neutrino mass of 1 eV. A reduced background rate has the largest impact on the η limit, almost improving it by a factor of 4. Note that in this case, the sensitivity limit derived by Kaboth et al. is reproduced [17]. An atomic tritium source would deliver a 35% improvement, and the MTD another 20%. If all three optimizations would be implemented at once, the η limit could almost be pushed below 1×10^9 .

Optimization	η limit, true $m_\nu = 1$ eV, 90% C.L.
None	8.6×10^9
MTD	7.0×10^9
Atomic source	5.5×10^9
Background rate 10 mcps	2.7×10^9
All 3 combined	1.1×10^9

Table 5.4: η limits at 90% C.L., calculated using KATRIN design fake MC with a true neutrino mass of 1 eV with different optimizations.

Chapter 6

KRN1 Exclusion Limit of the Relic Neutrino Overdensity

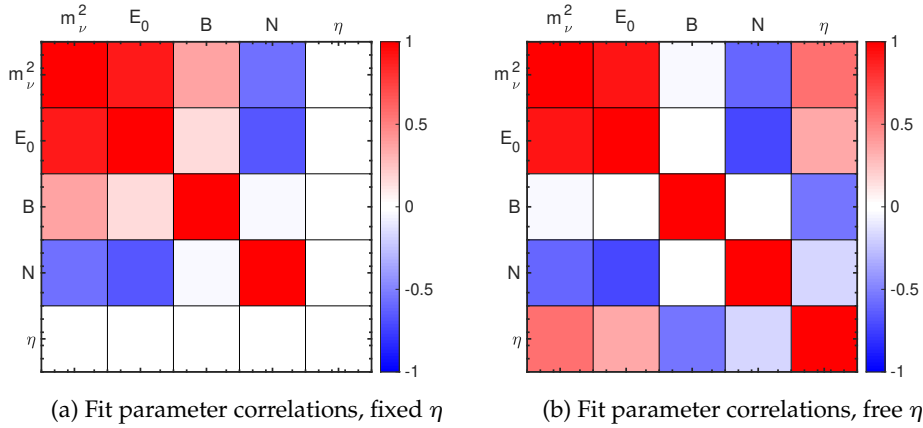
6.1 Best Fit Values

Tab. 6.1 shows all five fit parameters of the fit model, as well as the χ^2 , the number of degrees of freedom (dof) and the p-value. In the left column, η was fixed to zero. This case reproduces the KNM1 analysis, with the large negative neutrino mass squared of $m_\nu^2 = -1 \pm 0.97 \text{ eV}^2$. This negative m_ν^2 can be attributed to an excess of rate near the endpoint, which can be seen in Fig. 6.2 in the middle panel: The first three datapoints below $E=0$ lay clearly above the $\eta = 0$ fit. The right column of Tab. 6.1 contains the fit parameters with a free η . The same excess of rate leading to the negative m_ν^2 now leads to a large positive best fit of $\eta = 3.7 \pm 1.5 \cdot 10^{11}$. Fig. 6.2 illustrates how the fit follows the datapoints. Including η in the fit has an effect on all the other fit parameters as well, especially the neutrino mass. This is expected, since the high rate around the endpoint can now be fitted by the relic neutrino peak, and the neutrino mass directly determines the position of the relic peak. The η fit also has an impact on the correlations between the parameters, illustrated by Fig. 6.1: η is most strongly correlated with the neutrino mass, which explains the large change of the neutrino mass best fit when including η . Another strong correlation exists between η and the background rate, which weakens the correlations between the background rate and all other fit parameters that exist when η is fixed. The χ^2 improves by 3.73 by including the relic peak, so the fit is consistent with no relic neutrinos at 95% C.L. A χ^2 scan around the best fit value delivers an upper limit $\eta < 7 \times 10^{11}$ at 3σ C.L.

The best fit value of η on the data is surprisingly large compared to simulations with a true η of zero. Since all realistic predictions of η are essentially zero compared to our sensitivity (cf. Fig. 5.2), this is a good comparison to our expectation. Fig. 6.3 shows the distribution of η after 1000 fits on statistically fluctuated MC data sets with true $\eta = 0$ and true $m_\nu^2 = 0 \text{ eV}^2$ (shown above in Fig. 5.4), overlaid with the fraction of fit results greater than or equal to the fit result on data. If the relic neutrino overdensity is zero, then the probability of measuring an overdensity larger than $3.7 \cdot 10^{11}$ is 2.0%. While this is on the low end, it means that the result is not entirely incompatible with the simulations. The discrepancy might hence be partially explained by unlikely statistical fluctuations in the data set. Another factor could be the systematic effects from the source plasma and the penning trap between pre- and main spectrometer that were not taken into account in this data taking period (cf. Sec. 5.1.3).

	β decay only	β decay + $C\nu B$
m_ν^2	$-0.95 \pm 0.97 \text{ eV}^2$	$0.79 \pm 0.84 \text{ eV}^2$
E_0	$18573.73 \pm 0.06 \text{ eV}$	$18573.79 \pm 0.05 \text{ eV}$
N	0.990 ± 0.004	0.988 ± 0.003
B	$292.26 \pm 0.71 \text{ mcps}$	$291.45 \pm 0.83 \text{ mcps}$
η	0 (fixed)	$(3.7 \pm 1.5) \cdot 10^{11}$
χ^2/dof	21.7/23	17.9/22
p-val.	0.54	0.71

Table 6.1: Fit parameters on KRN1 data with and without relic neutrino peak

Figure 6.1: Correlations of the fit parameters for the KRN1 real data fit. η is most strongly correlated with the background and the neutrino mass. It also absorbs almost all correlations of the background with other fit parameters.

6.2 Possible Dependencies of the Best Fit Values

To investigate a possible time dependency of the η best fit value, the KRN1 data set was partitioned into three parts, each containing approximately 1/3 of the total statistics, sorted according to their time of recording. The associated run numbers of each list are provided in appendix B. There was no significant time dependency found, with η fluctuating 22% around the global best fit value, which is compatible with the 1σ uncertainty of η on the entire data set (cf. Tab. 6.1). Tab. 6.2 shows the three fit results for the three run lists.

Run list	η best fit
KNM1-FirstHalfTime	$3.6 \times 10^{11} \pm 2.8 \times 10^{11}$
KNM1-MiddleHalfTime	$4.5 \times 10^{11} \pm 2.4 \times 10^{11}$
KNM1-LastHalfTime	$2.9 \times 10^{11} \pm 2.8 \times 10^{11}$

Table 6.2: Time dependent η fit values

The pixels of the KATRIN detector are arranged in concentric rings around the beam line center, which allows for radial dependent fits. There are 14 rings in total, of which only 13 have active pixels in KRN1. For this analysis,

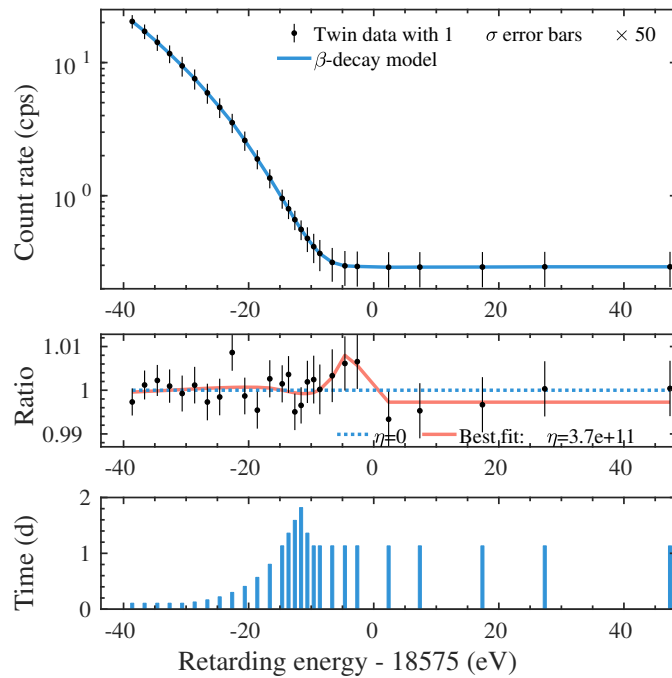


Figure 6.2: Best fit on KRN1 data including η , compared to the case without η .

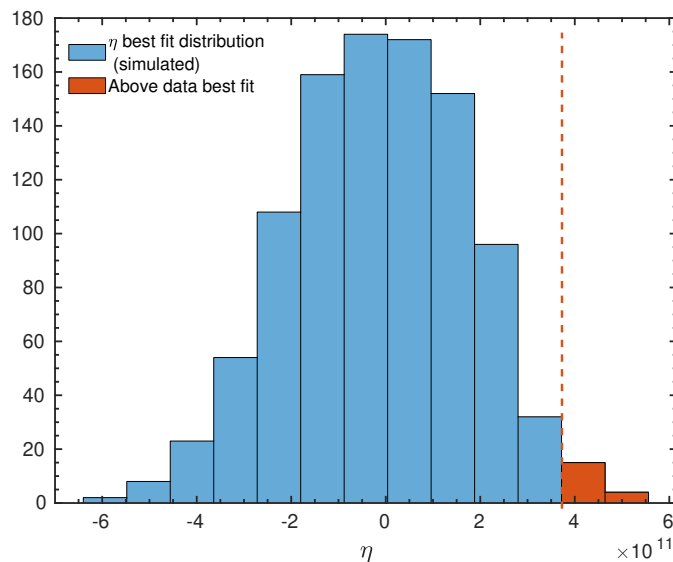


Figure 6.3: Fraction of η best fit values on fluctuated KRN1 MC above the KRN1 data best fit.

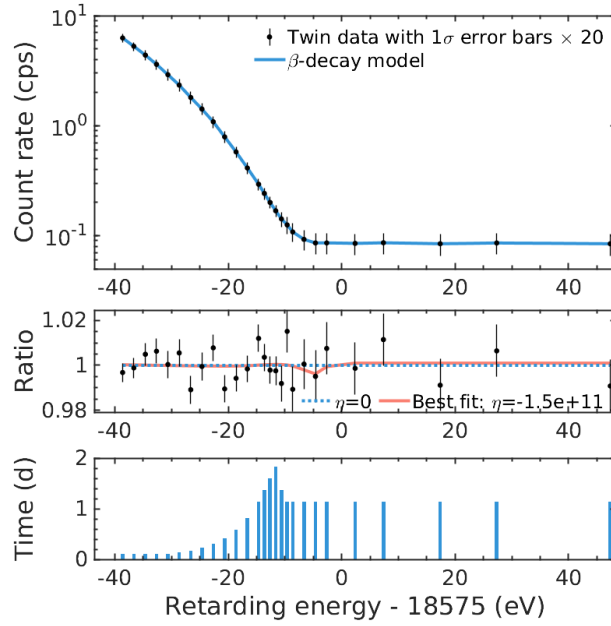


Figure 6.4: Spectrum and fit of PSR2 only

the rings were merged into 4 pseudo-rings (PSR): the innermost spans the rings 1, 2 and 3 with 28 active pixels, PSR2 contains the rings 4, 5 and 6 with 36 pixels, PSR3 the rings 7, 8 and 9 with 33 pixels, and the outermost PSR 4 merges the rings 10, 11, 12 and 13 with 20 active pixels. While PSR 1, 3 and 4 give slightly larger but quite consistent η fits of around 5×10^{11} , the second PSR deviates significantly with a slightly negative η best fit which is compatible with zero at $\eta = -1.5 \times 10^{11} \pm 3.4 \times 10^{11}$. The spectrum from PSR2 is depicted in Fig. 6.4. One data point, 4.5V below the endpoint, is responsible for the difference: it reliably lays above the fit with η fixed to zero for all other PSRs except for the second one, where it is located slightly below. The largest tension exists between PSR 2 and 3 at 2.3σ , which is not unusual: a set of 4 random numbers from the same Gaussian distribution should contain a tension of at least this size in around 25% of cases. If the 4 pseudo-rings are merged into two rings, one inner and one outer, there exists a slight radial trend to larger η values from the inner to the outer ring. Tab. 6.3 contains all PSR-wise η values and their uncertainties.

PSR	η best fit
1	$4.5 \times 10^{11} \pm 2.7 \times 10^{11}$
2	$-1.5 \times 10^{11} \pm 3.4 \times 10^{11}$
3	$5.4 \times 10^{11} \pm 2.6 \times 10^{11}$
4	$5.6 \times 10^{11} \pm 4.7 \times 10^{11}$

Table 6.3: η fit results, pseudo-ring wise

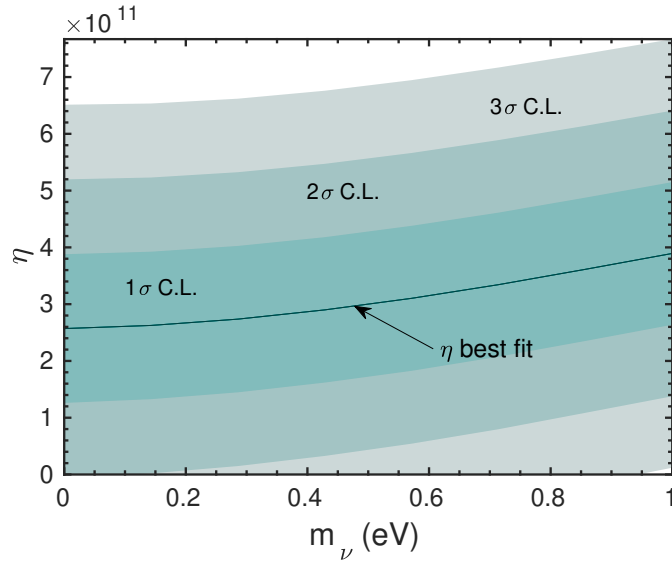


Figure 6.5: Raster scan over KRN1 data: η best fit value with 1, 2 and 3 σ confidence bounds vs. fixed neutrino mass.

6.3 Raster Scan

The raster scan, depicted in Fig. 6.5, was done over a neutrino mass range of $0 \text{ eV} \leq m_\nu \leq 1 \text{ eV}$, over which the fitted η value increases from 2.6×10^{11} to 3.8×10^{11} . As expected, due to the excess of rate near the endpoint, η is more than 2σ removed from zero over almost the entire neutrino mass range. The 3σ upper limit ranges from 6.5×10^{11} to 7.7×10^{11} , giving a global upper limit of $\eta < 7.7 \times 10^{11}$.

6.4 2D Scan

The 2D scan includes a region of non-physical neutrino mass, ranging from -1 eV^2 to 1 eV^2 . Fig. 6.6 shows the location of the global best fit and the contours at 90%, 95% and 99%, corresponding to a $\Delta\chi^2$ of 4.61, 5.99 and 9.21 respectively. The contours are elongated towards negative m_ν^2 , showing slight kinks at $m_\nu^2 = 0$. This is most likely due to the relic peak position not moving towards negative neutrino masses, but being fixed at $E_0 - 1.7 \text{ eV}$ in this region (see Sec. 3.3 for a detailed explanation). This keeps the relic peak more separated from the endpoint, improving the quality of the fit and subsequently enlarging the contours in the parameter space. The 99% contour in the positive neutrino mass range (highlighted in Fig 6.6) can be considered the final result of this analysis, with a global upper limit of $\eta < 7 \times 10^{11}$ at $m_\nu = 1 \text{ eV}$. Future neutrino mass limits such as the KATRIN KNM2 analysis will narrow this range down further.

6.5 Systematics Breakdown

The systematics breakdown (shown in Fig. 6.7) was conducted analogously to the one done on the twins in Sec. 5.1.3. The leading contributions (statistical uncertainty and background rate) as well as the total uncertainty

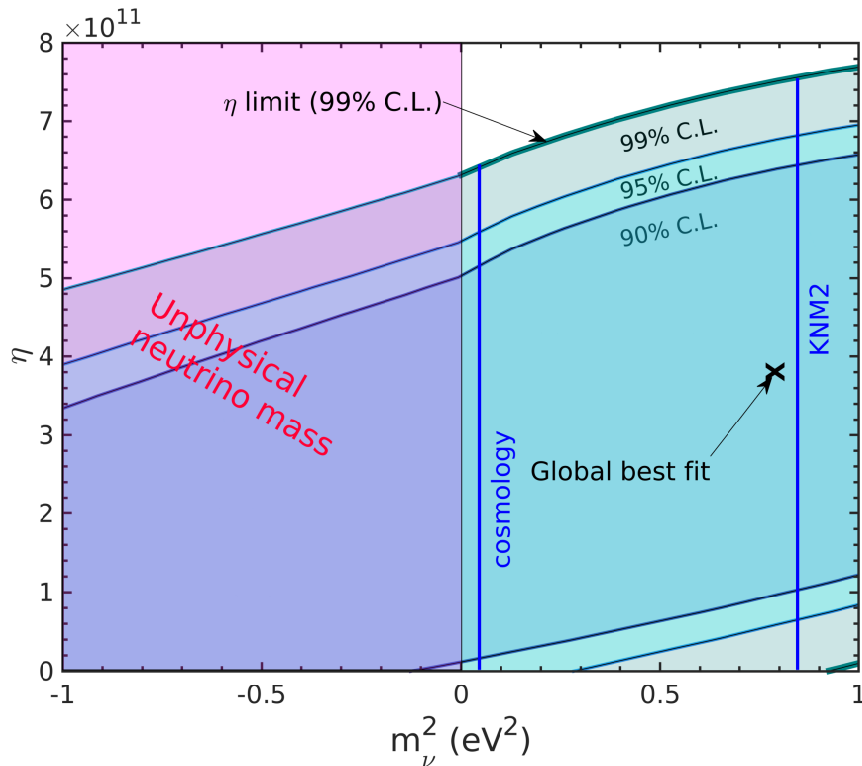
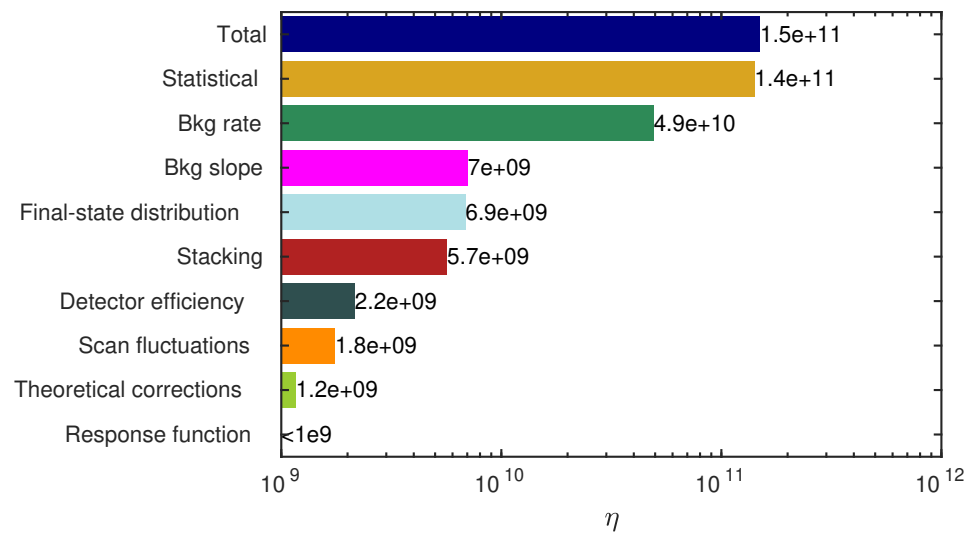


Figure 6.6: 2D scan over KRN1 data, showing 90%, 95% and 99% contours around the global best fit. Neutrino mass limits from KATRIN KNM2 and cosmology are shown as well.

match their predictions shown in Fig. 5.5 to more than 90%. Only the smaller contributions in the percentage range differ somewhat from the prediction, most notably the response function, which does not have any discernible effect on the systematics. For the twins, it contributed approx. 1% of the total uncertainty (cf. Fig. 5.5).

Figure 6.7: η systematics breakdown on KRN1 data

Chapter 7

Conclusions and Outlook

In this thesis, a relic neutrino model was developed and successfully implemented in the Samak analysis framework for the KATRIN experiment. It was subsequently used to determine the expected sensitivity on the local relic neutrino overdensity η , both of the existing KRN1 data set and the KATRIN experiment after its full runtime. The sensitivity of KRN1 is predicted to be about $\eta < 3 \times 10^{11}$ at 90% C.L., which is an improvement over the limit derived by the Troitsk experiment in 1999. The KRN1 sensitivity is statistics dominated, with the leading systematic effects being the background rate. The detailed modeling of the tritium beta spectrum only has a modest impact on the sensitivity, contrary to the neutrino mass and sterile neutrino analyses. The final sensitivity limit of KATRIN (assuming 1000 days of data and a background of 130 mcps, cf. [1]) is about $\eta < 1 \times 10^{10}$, which is an order of magnitude larger compared to previous estimates such as [17]. This is mainly due to the elevated background compared to the KATRIN design report [7]. In a second stage, the KRN1 data was analyzed, with no evidence of a relic neutrino signal (or more precisely, its overdensity) being found. The best fit result of $\eta = 3.7 \pm 1.5 \times 10^{11}$ represents a 2σ fluctuation from the expectation, with a p-value of 2%. This is due to statistical fluctuations that also led to the negative neutrino mass best fit in KRN1. No temporal or radial dependencies were found for the best fit. The most important systematic contributions to the uncertainty match their predictions from simulations to more than 90%. The main result is the 99% upper limit on the relic neutrino overdensity η for neutrino masses below 1 eV, as shown in Fig. 6.6. This result is translated into an upper limit of $\eta < 7 \cdot 10^{11}$ at 99% C.L., which is still more stringent than the limit on the relic neutrino overdensity obtained at Troitsk. Using the precise data from KATRIN, this work aims to serve as a proof of concept for future relic neutrino searches with tritium-based direct kinematics experiments, and more importantly to serve as a precursor to subsequent KATRIN analyses that will incorporate more data. This is an exciting avenue to pursue, as KATRIN should improve the relic neutrino overdensity limit by at least an order of magnitude after its entire runtime.

Acknowledgements

I want to express my sincere gratitude towards all the people that helped me make this analysis a reality. First and foremost, I would like to thank Prof. Susanne Mertens for providing me with the opportunity to be a part of the KATRIN collaboration and to work on this interesting and rewarding topic. Next, I am very thankful to my supervisor during this task, Dr. Thierry Lasserre, for the regular support and valuable input, and also to Lisa Schlüter, for introducing me to MATLAB and always being ready to help out with coding problems and other questions. Thirdly, I want to thank all the members of our group at the MPP for the friendly and open work environment. Although it was often necessary to work from home, it was always a pleasure to return to the office. Lastly, I owe my gratitude to all readers and correctors of this thesis.

Bibliography

- [1] M. Aker et al. “Bound on 3+1 Active-Sterile Neutrino Mixing from the First Four-Week Science Run of KATRIN”. In: *Physical Review Letters* 126.9 (2021). issn: 1079-7114. doi: [10.1103/physrevlett.126.091803](https://doi.org/10.1103/physrevlett.126.091803). url: <http://dx.doi.org/10.1103/PhysRevLett.126.091803>.
- [2] M. Aker et al. *First direct neutrino-mass measurement with sub-eV sensitivity*. 2021. arXiv: [2105.08533](https://arxiv.org/abs/2105.08533) [hep-ex].
- [3] M. Aker et al. “Improved Upper Limit on the Neutrino Mass from a Direct Kinematic Method by KATRIN”. In: *Physical Review Letters* 123.22 (2019). issn: 1079-7114. doi: [10.1103/physrevlett.123.221802](https://doi.org/10.1103/physrevlett.123.221802). url: <http://dx.doi.org/10.1103/PhysRevLett.123.221802>.
- [4] Ali Ashtari Esfahani et al. “Determining the neutrino mass with cyclotron radiation emission spectroscopy—Project 8”. In: *J. Phys. G* 44.5 (2017), p. 054004. doi: [10.1088/1361-6471/aa5b4f](https://doi.org/10.1088/1361-6471/aa5b4f). arXiv: [1703.02037](https://arxiv.org/abs/1703.02037) [physics.ins-det].
- [5] L. I. Bodine, D. S. Parno, and R. G. H. Robertson. “Assessment of molecular effects on neutrino mass measurements from tritium β decay”. In: *Phys. Rev. C* 91 (3 2015), p. 035505. doi: [10.1103/PhysRevC.91.035505](https://doi.org/10.1103/PhysRevC.91.035505). url: <https://link.aps.org/doi/10.1103/PhysRevC.91.035505>.
- [6] Alfredo G Cocco, Gianpiero Mangano, and Marcello Messina. “Probing low energy neutrino backgrounds with neutrino capture on beta decaying nuclei”. In: *Journal of Cosmology and Astroparticle Physics* 2007.06 (2007), pp. 015–015. doi: [10.1088/1475-7516/2007/06/015](https://doi.org/10.1088/1475-7516/2007/06/015). url: <https://doi.org/10.1088/1475-7516/2007/06/015>.
- [7] KATRIN Collaboration. *KATRIN design report 2004*. Tech. rep. 51.54.01; LK 01. Forschungszentrum Jülich, 2005. 245 pp. doi: [10.5445/IR/270060419](https://doi.org/10.5445/IR/270060419).
- [8] Amand Faessler et al. “Beta Decay and the Cosmic Neutrino Background”. In: *EPJ Web of Conferences* 71 (Apr. 2014), p. 00044. doi: [10.1051/epjconf/20147100044](https://doi.org/10.1051/epjconf/20147100044).
- [9] Amand Faessler et al. “Can one measure the Cosmic Neutrino Background?” In: *International Journal of Modern Physics E* 26.01n02 (2017), p. 1740008. issn: 1793-6608. doi: [10.1142/S0218301317400080](https://doi.org/10.1142/S0218301317400080). url: <http://dx.doi.org/10.1142/S0218301317400080>.
- [10] Amand Faessler et al. *Search for the Cosmic Neutrino Background and KATRIN*. 2013. arXiv: [1304.5632](https://arxiv.org/abs/1304.5632) [nucl-th].

- [11] G.L. Fogli et al. "Neutrino oscillations: Global analyses". In: *Nuclear Physics B - Proceedings Supplements* 118 (2003), 177–186. issn: 0920-5632. doi: [10.1016/S0920-5632\(03\)01315-X](https://doi.org/10.1016/S0920-5632(03)01315-X). url: [http://dx.doi.org/10.1016/S0920-5632\(03\)01315-X](http://dx.doi.org/10.1016/S0920-5632(03)01315-X).
- [12] Steen Hannestad. "Primordial Neutrinos". In: *Annual Review of Nuclear and Particle Science* 56.1 (2006), 137–161. issn: 1545-4134. doi: [10.1146/annurev.nucl.56.080805.140548](https://doi.org/10.1146/annurev.nucl.56.080805.140548). url: <http://dx.doi.org/10.1146/annurev.nucl.56.080805.140548>.
- [13] Rastislav Hodak et al. *Beta Decaying Nuclei as a Probe of Cosmic Neutrino Background*. 2011. arXiv: [1102.1799](https://arxiv.org/abs/1102.1799) [hep-ph].
- [14] W-Y P Hwang and Bo-Qiang Ma. "Detection of cosmic neutrino clustering by cosmic ray spectra". In: *New Journal of Physics* 7 (2005), pp. 41–41. doi: [10.1088/1367-2630/7/1/041](https://doi.org/10.1088/1367-2630/7/1/041). url: <https://doi.org/10.1088/1367-2630/7/1/041>.
- [15] *IceCube*. url: <https://icecube.wisc.edu/>.
- [16] *JEM-EUSO*. url: <https://www.jemeuso.org/>.
- [17] A. Kaboth, J. A. Formaggio, and B. Monreal. "Sensitivity of neutrino mass experiments to the cosmic neutrino background". In: *Physical Review D* 82.6 (2010). issn: 1550-2368. doi: [10.1103/PhysRevD.82.062001](https://doi.org/10.1103/PhysRevD.82.062001). url: <http://dx.doi.org/10.1103/PhysRevD.82.062001>.
- [18] M. Kleesiek et al. " β -Decay spectrum, response function and statistical model for neutrino mass measurements with the KATRIN experiment". In: *The European Physical Journal C* 79.3 (2019). issn: 1434-6052. doi: [10.1140/epjc/s10052-019-6686-7](https://doi.org/10.1140/epjc/s10052-019-6686-7). url: <http://dx.doi.org/10.1140/epjc/s10052-019-6686-7>.
- [19] *KM3NeT*. url: <https://www.km3net.org/>.
- [20] R Lazauskas, P Vogel, and C Volpe. "Charged current cross section for massive cosmological neutrinos impinging on radioactive nuclei". In: *Journal of Physics G: Nuclear and Particle Physics* 35.2 (2007), p. 025001. doi: [10.1088/0954-3899/35/2/025001](https://doi.org/10.1088/0954-3899/35/2/025001). url: <https://doi.org/10.1088/0954-3899/35/2/025001>.
- [21] V.M. Lobashev et al. "Neutrino mass and anomaly in the tritium beta-spectrum. Results of the "Troitsk ν -mass" experiment". In: *Nuclear Physics B - Proceedings Supplements* 77.1 (1999), pp. 327–332. issn: 0920-5632. doi: [https://doi.org/10.1016/S0920-5632\(99\)00438-7](https://doi.org/10.1016/S0920-5632(99)00438-7). url: <https://www.sciencedirect.com/science/article/pii/S0920563299004387>.
- [22] Julio F. Navarro, Carlos S. Frenk, and Simon D. M. White. "The Structure of Cold Dark Matter Halos". In: *The Astrophysical Journal* 462 (1996), p. 563. issn: 1538-4357. doi: [10.1086/177173](https://doi.org/10.1086/177173). url: <http://dx.doi.org/10.1086/177173>.
- [23] J I Read. "The local dark matter density". In: *Journal of Physics G: Nuclear and Particle Physics* 41.6 (2014), p. 063101. issn: 1361-6471. doi: [10.1088/0954-3899/41/6/063101](https://doi.org/10.1088/0954-3899/41/6/063101). url: <http://dx.doi.org/10.1088/0954-3899/41/6/063101>.

- [24] Andreas Ringwald. "How to Detect Big Bang Relic Neutrinos?" In: (2005). arXiv: [hep-ph/0505024](https://arxiv.org/abs/hep-ph/0505024) [hep-ph].
- [25] Andreas Ringwald and Yvonne Y Y Wong. "Gravitational clustering of relic neutrinos and implications for their detection". In: *Journal of Cosmology and Astroparticle Physics* 2004.12 (2004), pp. 005–005. doi: [10.1088/1475-7516/2004/12/005](https://doi.org/10.1088/1475-7516/2004/12/005). url: <https://doi.org/10.1088/1475-7516/2004/12/005>.
- [26] R. G. H. Robertson et al. "Limit on ν_e mass from observation of the β decay of molecular tritium". In: *Phys. Rev. Lett.* 67 (8 1991), pp. 957–960. doi: [10.1103/PhysRevLett.67.957](https://link.aps.org/doi/10.1103/PhysRevLett.67.957). url: <https://link.aps.org/doi/10.1103/PhysRevLett.67.957>.
- [27] Alejandro Saenz, Svante Jonsell, and Piotr Froelich. "Improved Molecular Final-State Distribution of HeT⁺ for the β -Decay Process of T₂". In: *Phys. Rev. Lett.* 84 (2 2000), pp. 242–245. doi: [10.1103/PhysRevLett.84.242](https://link.aps.org/doi/10.1103/PhysRevLett.84.242). url: <https://link.aps.org/doi/10.1103/PhysRevLett.84.242>.
- [28] S. Sangiorgio. "The microcalorimeter arrays for a Rhenium experiment (MARE): A next-generation calorimetric neutrino mass experiment based on the study of ¹⁸⁷Re β spectrum". In: *Prog. Part. Nucl. Phys.* 57 (2006). Ed. by A. Faessler, pp. 68–70. doi: [10.1016/j.pnpnp.2005.11.004](https://doi.org/10.1016/j.pnpnp.2005.11.004).
- [29] G. J. Stephenson, T. Goldman, and B. H. J. McKellar. "Neutrino Clouds". In: *International Journal of Modern Physics A* 13.16 (1998), 2765–2790. issn: 1793-656X. doi: [10.1142/S0217751X98001414](https://dx.doi.org/10.1142/S0217751X98001414). url: <http://dx.doi.org/10.1142/S0217751X98001414>.
- [30] Mihran Vardanyan, Roberto Trotta, and Joseph Silk. "How flat can you get? A model comparison perspective on the curvature of the Universe". In: *Monthly Notices of the Royal Astronomical Society* 397.1 (2009), 431–444. issn: 1365-2966. doi: [10.1111/j.1365-2966.2009.14938.x](https://doi.org/10.1111/j.1365-2966.2009.14938.x). url: <http://dx.doi.org/10.1111/j.1365-2966.2009.14938.x>.
- [31] Christian Weinheimer et al. "The Mainz neutrino mass experiment". In: (Dec. 2001), p. 192. doi: [10.22323/1.007.0192](https://doi.org/10.22323/1.007.0192).
- [32] P.A. Zyla et al. "Review of Particle Physics". In: *PTEP* 2020.8 (2020), p. 083C01. doi: [10.1093/ptep/ptaa104](https://doi.org/10.1093/ptep/ptaa104).

Appendix A

Associated Code

Code Repository:

<https://nuserv.uni-muenster.de:8443/LSchlueter/Samak3.0>

Macro used for generating the main plots:

FinalPlot.m

Appendix B

Time-specific sub-samples of the KRN1 golden Run List

B.1 KNM1-FirstHalfTime (92 runs)

1410 5141151412 51413 51414 51415 51416 51417 51418 51419 51420 51421
 51422 51423 51424 51425 5142651441 51442 51443 51444 51446 51447 51448
 51449 51450 51451 51452 51453 51454 51455 5145651457 51458 51459 51460
 51461 51462 51463 51464 51465 51466 51467 51468 51469 51470 5147251473
 51474 51475 51476 51477 51478 51479 51480 51481 51486 51487 51488 51489
 51490 5149151492 51493 51494 51495 51496 51497 51498 51499 51500 51501
 51502 51503 51516 51517 5152151522 51523 51524 51525 51526 51527 51528
 51529 51530 51531 51532 51533 51534 51535 51536

B.2 KNM1-MiddleHalfTime (91 runs)

1537 5153851539 51540 51541 51542 51543 51544 51545 51546 51547 51548
 51549 51550 51551 51552 5155351554 51555 51556 51557 51558 51559 51560
 51561 51562 51563 51564 51565 51566 51579 5158051581 51582 51583 51584
 51585 51586 51639 51640 51641 51642 51643 51644 51645 51646 5164751651
 51652 51653 51654 51655 51656 51657 51658 51659 51660 51664 51665 51669
 51670 5167151672 51673 51674 51675 51676 51677 51678 51679 51680 51681
 51682 51683 51684 51685 5168651687 51688 51689 51690 51692 51693 51694
 51695 51696 51701 51703 51704 51705 51706

B.3 KNM1-LastHalfTime (91 runs)

1707 5170851709 51822 51823 51824 51825 51826 51827 51828 51829 51830
 51831 51832 51833 51834 5183551836 51837 51838 51839 51840 51841 51842
 51843 51844 51845 51846 51847 51848 51849 5185051851 51852 51853 51854
 51855 51856 51857 51858 51859 51860 51870 51871 51872 51873 5187451875
 51876 51879 51880 51881 51882 51883 51884 51885 51886 51887 51888 51889
 51890 51891 51892 51893 51894 51895 51898 51908 51909 51910 51911 51912
 51913 51919 51920 51921 5192251923 51924 51925 51926 51927 51928 51929
 51930 51931 51932 51933 51934 51935 51936